J. Mol. Biol. (1993) **229**, 1101–1124

Nicotinic Acetylcholine Receptor at 9 Å Resolution

N. Unwin

MRC Laboratory of Molecular Biology
Hills Road, Cambridge CB2 2QH, U.K.

(Received 6 October 1992; accepted 26 November 1992)

The nicotinic acetylcholine receptor is a cation-selective, ligand-gated ion channel, involved in signal transmission at the chemical synapse. This paper reports the three-dimensional appearance of the channel in the closed conformation, at 9 Å resolution. The structure was determined by electron microscopy of tubular crystals of *Torpedo* postsynaptic membranes embedded in amorphous ice.

The analysis was carried out by averaging data from separate images, using helical diffraction methods. The images were recorded over a wide range of defocus (7000 to 18,800 Å) so that all spacings in the object were well sampled. Tubes of only one kind ((−16,6) helical family) were processed, so that the Fourier terms could be averaged directly in reciprocal space. The three-dimensional map, obtained from 26 images, resolves some elements of secondary structure within the five protein subunits.

In the synaptic part of each subunit, about 30 Å from the bilayer surface, there is a group of three rods that are oriented predominantly perpendicular to the plane of the bilayer and twist around each other as in a left-handed coil. These rods presumably are α-helices. Two of them line the entrance to the channel, and the third is on the outside. The distinctive appearance of the α subunits in this region suggests that the rods may be involved in forming the binding pocket for acetylcholine.

In the bilayer-spanning part of each subunit there is only one rod clearly visible, which forms the wall lining the pore, and so is assumed to be the transmembrane helix, M2. This rod does not form a straight path through the lipid bilayer, but bends, or kinks, near its mid-point, where it is closest to the axis of the pore, and tilts radially outwards on either side. It is flanked on the lipid-facing sides by a continuous rim of density, which seems likely to be composed of β-sheet.

A tentative alignment is made between the three-dimensional densities and the sequence of M2, based on correlation of the appearance of the rods with a special pattern of amino acid residues in the sequence. This alignment places the charged groups at the ends of M2 symmetrically on either side of the bilayer, and a highly conserved leucine residue (Leu251 of the α subunit) at the level of the kink. It is suggested that leucine side-chains projecting into the pore from the kinks associate and create a tight hydrophobic ring, which closes the channel by making a barrier that hydrated ions cannot cross.

Keywords: acetylcholine receptor; ion channel; cryo-electron microscopy; helical analysis

1. Introduction

The acetylcholine receptor at the neuromuscular junction, and in the electroplaque membranes of *Torpedo* rays, is the best-characterized member of a family of neurotransmitter-gated ion channels, which includes the neuronal acetycholine receptor, the $GABA_A$ receptor, the glycine receptor and the 5HT-3 (serotonin) receptor. It is composed of a ring of five membrane-spanning subunits (α, α, β, γ and δ) which together delineate a central, cation-conducting pathway. This channel opens transiently when acetylcholine is released from the nerve terminal into the synaptic cleft, and depolarizes the postsynaptic membrane. The function of the receptor is thus to convert rapidly a chemical signal from one cell into an electrical signal that is propagated along the membrane of the next.

Much of our current understanding of this protein is based on amino acid sequence information, data obtained from pharmacological and biochemical studies, and the results of site-directed mutagenesis experiments combined with electrophysiological study of function (for recent reviews, see Claudio, 1989; Galzi *et al.*, 1991; Karlin, 1991). Only the α subunits bind acetylcholine to open the channel, but

0022-2836/93/041101-24 $08.00/0

the other subunits have similar amino acid sequences (about 40% identity), indicating that their tertiary folding is very similar. The polypeptides vary in length between 437 (α) and 501 (δ) amino acid residues, and there are four significant hydrophobic stretches within each sequence. Although the topology relative to the membrane has not yet been determined unambiguously, it is thought that these hydrophobic stretches correspond to transmembrane segments (M1 to M4). A considerable body of evidence now indicates that the long N-terminal domain and short C-terminal tail are on the synaptic side, and that the short link between M1 and M2 and the longer link between M3 and M4 are on the cytoplasmic side.

It is usually assumed that the segments of the polypeptides crossing the bilayer are α-helices (Noda *et al.*, 1983*b*). But the nature of the secondary structure inside the membrane has not been explored directly by experiment. Circular dichroism measurements indicate that the receptor may have only about 23% of its mass in the α-helical configuration (Mielke & Wallace, 1988), which is hardly enough to account for a four-α-helical transmembrane structure if the molecule contains α-helices in other parts. X-ray diffraction patterns from partially oriented membrane samples have been interpreted to indicate that the whole molecule contains α-helices that are 80 Å (1 Å = 0·1 nm) in length (Ross *et al.*, 1977; Kistler *et al.*, 1982).

Functional analyses of mutant acetylcholine receptors expressed in *Xenopus* oocytes have demonstrated that amino acid residues flanking and within the putative α-helix, M2, have specific effects related to ion transport; they are therefore located close to, or within the narrow part of the conduction pathway (Imoto *et al.*, 1988; Leonard *et al.*, 1988; Charnet *et al.*, 1990; Villarroel *et al.*, 1991; Villarroel & Sakmann, 1992; Akabas *et al.*, 1992). Photolabelling studies, using channel blocking reagents such as chlorpromazine and triphenylmethylphosphonium, have also stressed the involvement of M2, since these compounds bind to specific residues of different subunits at homologous positions in the M2 sequence (Giraudat *et al.*, 1986,1987; Hucho *et al.*, 1986; Revah *et al.*, 1990; Pedersen *et al.*, 1992). Another region of the sequence, at the N-terminal end of M1, is labelled by the open channel blocker, quinacrine azide (DiPaola *et al.*, 1990). Thus other parts of the sequence may also contribute to the narrow part of the pathway.

The quaternary structure of the receptor has been investigated by electron microscopy of isolated and membrane-bound molecules, using negative staining (Zingsheim *et al.*, 1980; Kistler & Stroud, 1981; Bon *et al.*, 1984; Brisson & Unwin, 1984; Kubalek *et al.*, 1987; Mitra *et al.*, 1989) and rapid freezing (Brisson & Unwin, 1985; Unwin *et al.*, 1988; Toyoshima & Unwin, 1988*a*, 1990) as a means of structure preservation. *Torpedo* postsynaptic membrane has been an invaluable source of material for this work, and tubular crystals of these membranes, analysed by rapid freezing and cryo-electron microscopy, have so far provided the most detailed picture. The structure determined at 17 Å resolution (Toyoshima & Unwin, 1988*a*, 1990) shows that the subunits are 120 Å long rods, arranged around a pseudo-5-fold axis and lying approximately normal to the membrane plane. The conduction pathway, delineated by the pseudo-symmetry axis, is seen to consist of a narrow pore across the bilayer, bounded by 20 to 25 Å wide entrances that extend 60 Å towards the synapse and 20 Å towards the interior of the cell. Although various models have been proposed, it is not known exactly how the pore is formed by the M2 segments and other parts of the sequence.

The tertiary folding of the protein subunits is of considerable interest, since this knowledge would provide a three-dimensional framework on which to base the extensive chemical and physical data, including the results of the labelling and site-directed mutagenesis experiments cited above. We have therefore begun an investigation of the tubular crystals at higher resolution by recording images of them at different levels of defocus to obtain partial but complementary data (Unwin & Henderson, 1975), and deriving from these data by helical analysis (DeRosier & Klug, 1968; Jeng *et al.*, 1989) a full set of three-dimensional terms. This method of analysis is similar to that used to determine structure from planar crystals (Henderson & Unwin, 1975; Henderson *et al.*, 1990), except that, because of the helical symmetry, all necessary views are present and no tilting of the specimen is required.

A description is presented here of the receptor, in the closed conformation, at a resolution of 9 Å. It is possible now to resolve some elements of secondary structure. A group of three rods is visualized in the synaptic part of each subunit, about 30 Å above the bilayer surface. The two α subunits have a distinctive appearance in this region, suggesting that the rods may be involved in forming the binding pocket for acetylcholine. Another rod is seen in the bilayer-spanning part of each subunit, which forms the wall lining the pore. Features of these rods, which probably are α-helices, provide insight into how the acetylcholine binding site might be designed and how the gate of the closed channel might be constructed.

2. Experimental

(a) *Electron microscopy*

Tubular crystals composed of acetylcholine receptors in their native lipid/protein environment were grown from *Torpedo marmorata* postsynaptic membranes (Kubalek *et al.*, 1987), using fish caught in the autumn or winter. Only about 1 in 10 fish provided tubes that were straight, narrow, and in high yield as required for further study.

Portions (5 μl) of solution containing the tubes were applied to the carbon side of holey carbon support grids. Excess solution was blotted off, usually from the grid side (Toyoshima, 1989), and the grids were plunged into liquid ethane slush to embed the specimens in amorphous ice. The grids were stored in liquid nitrogen. Specimens were

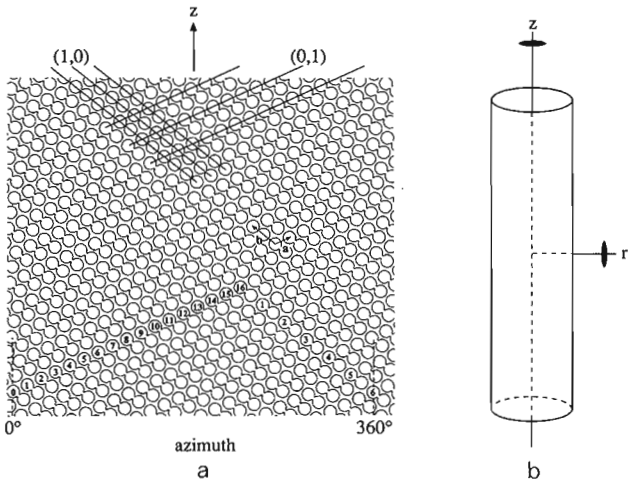

Figure 1. Surface lattice (a), and (b) symmetry elements for the (−16,6) family of tube. The surface lattice is built from dimers of receptors (linked circles) arranged with p2 plane group symmetry (Brisson & Unwin, 1984). The unit cell vectors of this lattice and the 1,0 and 0,1 lines are indicated. The (−16,6) tube is characterized by the fact that it has 16 1,0 and 6 0,1 lines filling 360° of azimuth (i.e. the start numbers of the principal left-handed 1,0 and right-handed 0,1 helices are −16 and 6, respectively). This particular packing of receptors generates a 2-fold rotation axis along the central axis of the tube and 4 kinds of radial 2-fold axes (only one of which is shown).

examined at low temperature (−168 to −180°C), using Gatan cryo-holders and Philips EM400, EM420, CM12 and CM20 electron microscopes, all equipped with twin lenses, twin-bladed anticontaminators and low dose facilities. Coherent illumination was achieved by making the diameter of the second condenser aperture small (50 μm) and by strongly exciting the first condenser lens. A thin foil 50 μm diameter objective aperture was always in place.

The search for suitable specimens was carried out in the defocused diffraction mode (magnification ~1000×). Tubes had to appear thin and straight within the holes of the carbon support film, and the ice around them had to appear thick enough to make flattening unlikely. Electron micrographs were recorded with low doses at 120 or (in one case) 200 kV, using nominal magnifications of 35,000 to 40,000× and 1 s exposure times. The magnification was held constant with any particular microscope by adjusting the height of the cryo-holder to maintain a constant objective lens current. Vibration of the specimen during recording was minimized by operating the cryo-holder under conditions where there was no bubbling of the liquid nitrogen in the dewar; movement of the specimen was minimized by using the heater control to compensate for drift. The film was Kodak S0-163, which was developed for 12 min in D19 developer. The total electron dose given to each image, estimated from the optical density of the film, was 6 to 8 electrons/Å^2.

(b) *Selection of images*

The present analysis is concerned just with the (−16,6) helical family of tube (Fig. 1; Toyoshima & Unwin, 1990), which is one of many families in a typical preparation. Micrographs were screened for the (−16,6) tubes by optical diffraction. The criteria for image quality were as described (Toyoshima & Unwin, 1988*a*, 1990). The diffraction patterns had to be symmetrical, indicating that the tube was properly embedded in the ice, astigmatism had to be minimal and the diffraction had to extend to high resolution. Contrast transfer function modulations ("Thon rings"; Thon, 1966) were weakly visible in the background diffraction from boxed-off areas of the tubes, and their appearance was important in making this initial assessment of the images.

Selected micrographs were digitized with a flatbed microdensitometer manufactured by Joyce, Loebl and Co., Ltd (extensively modified in-house), using a scanning interval of 7·5 μm (corresponding to 2·15 Å on the specimen). Additional screening of the images was carried out on the basis of the computed Fourier transforms. Images were rejected if they gave layer-lines that were unsharp or that indicated, from their phases (DeRosier & Moore, 1970), strong tilting of the tube (>5°) away from the plane normal to the electron beam. In some cases the tubes appeared to be slightly flattened (see below); these images were also rejected.

(c) *Estimation of the contrast transfer function*

Contrast transfer functions (ctfs†) were estimated from the Fourier transforms of images of boxed-off lengths of tubes. The amplitudes at different radii were averaged over 5 separate 36° sectors, and over 180° sectors, and compared to theoretical curves, assuming 7% amplitude contrast (Fig. 2a; Toyoshima & Unwin, 1988*b*). For the images to be suitable for further analysis, the radial plots needed to show a series of maxima and minima extending to 1/8 Å^{-1}. If the maxima and minima were not visible in the 36° sector averages, or were visible but in inconsistent positions, the images were considered to have drift or astigmatism and were rejected. The accuracy of defocus measurement by matching of experimental and theoretical curves was about ±200 Å over the range of defocus values used (7000 to 18,800 Å, underfocus). Images recorded closer to focus than the lower limit of the range were not used because of the weakened contrast transfer at low resolution and difficulties in obtaining accurate 2-fold alignments; images recorded further from focus than the upper limit were not used because of the weakened contrast transfer at high resolution, due to the effect of partial coherence (Frank, 1973).

(d) *Image processing*

Because of the centrosymmetric nature of the tube, when viewed down a radial two-fold axis (Fig. 1), it was always possible to adjust the phase origin such that all phases should be 0° or 180°. Use was made of this property for aligning different datasets and to assess quality of data at various stages of the analysis. Another property of the tubes is that the helical repeat distance varies, so that different tubes have different helical selection rules. However, variations in the dimensions of the surface lattice were small in comparison with the resolution attainable (see Results, section (d)). Hence, it was possible to compare and combine datasets in reciprocal space, assuming a common helical selection rule, without introducing significant error.

With a few of the tubes (having the smallest repeat distances) the high-resolution Fourier terms along one layer-line overlapped with those along another (see Table 1); data were not collected where this occurred.

† Abbreviation used: ctf, contrast transfer function.

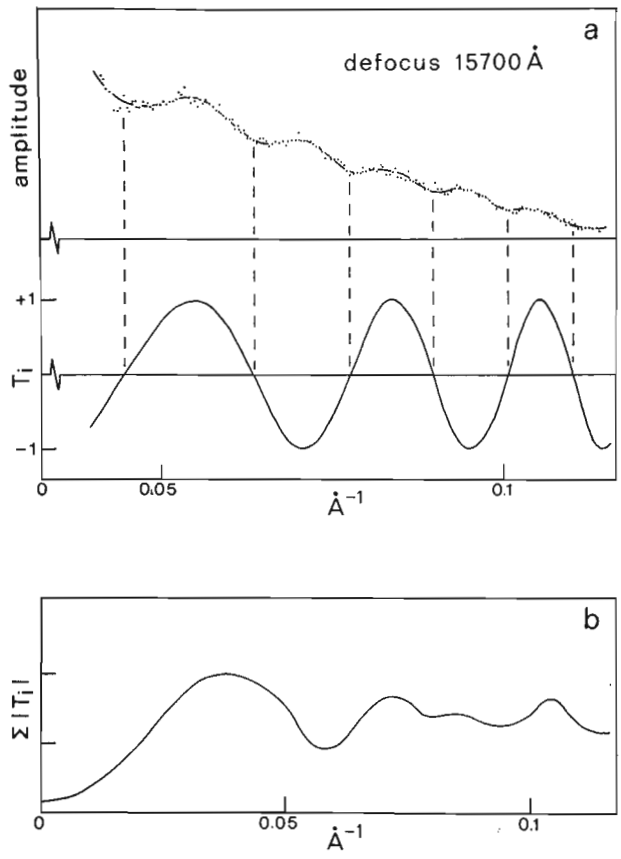

Figure 2. a, Estimation of the contrast transfer function by comparing the radial amplitude variation in the Fourier transform of an image of a tube (film 769; upper panel) with theoretical curves (lower panel). The amplitude profile, obtained by averaging over a sector of 180°, consists of a series of maxima and minima extending to high resolution (see also Fig. 4b). The positions of the zeros in the theoretical ctf for 15,700 Å underfocus match up closely with the positions of the observed minima, indicating the actual defocus of the image. b, Plot of the sum of the moduli of the ctfs from the 26 images used, demonstrating that all spacings for which the resolution is better than about 100 Å have been well sampled.

The alignment of the tube axis with respect to the box, the correction for tilt of the tube away from the plane normal to the electron beam, and the extraction of layer-lines from Fourier transforms were done by the same procedures as described (Toyoshima & Unwin, 1990), but using twice the array size (1024 × 2048). The manipulations entailed interpolation of each digitized image to include an integral multiple of the helical repeat distance, thus forcing all of the layer-lines in the Fourier transform to lie exactly on the sampling raster. Prior determination of the repeat distance and of the rotation angle of the tube with respect to the sampling raster are important steps in this procedure, and the initial values obtained for these parameters were refined in the present study to ensure that the fit of the layer-lines to the transform grid was optimized, and extended accurately to the highest resolution terms.

The refinement was conducted in 2 steps, first to obtain the best fit of the layer-lines to the transform grid in the Z direction (along the helix axis) and second, to obtain the best fit in the R direction (perpendicular to the helix axis). In the first step, the dimension of the box enclosing the tube was varied in increments of grid units (1 grid unit, 2·15 Å) around the value estimated to include a multiple of the repeat distance. Transforms were calculated for these different box sizes and, with each transform, plots were made of the amplitude variation along all the major, high Z, near-meridional layer-lines. The refined dimension of the box (i.e. the exact multiple of the repeat distance) was the dimension at which the strongest peaks on these layer-lines attained their highest values. In the second step, the rotation angle of the tube with respect to the sampling raster was varied in increments of 0·05° about the estimated value. The corresponding transforms were calculated, and the 2-fold phase residual for the layer-line data was determined for each case (using just the layer-line data out to the first minimum of the ctf). The refined rotation angle was the value at which the 2-fold phase residual was smallest.

These refinements led typically to an accuracy of better than 0·05% and 0·05° in the figures for the repeat distance and rotation angle, respectively.

(e) *Merging of datasets*

Datasets from each image consisted of all possible layer-lines (total number: 287) to a resolution of 8·7 Å. Usually, the datasets were obtained by averaging the Fourier terms from 2 or 3 transforms of contiguous or overlapping stretches along a tube.

Before these datasets could be combined vectorially to create a single, average dataset, a fitting procedure had to be applied to bring each of them to a common 2-fold phase origin, and to provide consistent scaling in the radial direction. Also, the layer-lines composing each dataset had to be reassigned according to a common helical selection rule.

The fitting procedure used data just to the first zero of the ctf. It involved minimization of the phase residual, ϕ_f, between test and reference datasets, using the relation (Amos & Klug, 1975):

$$\phi_f = \sqrt{\frac{\Sigma|F_{ref}(R,l)|\cdot\delta\phi(R,l)^2}{\Sigma|F_{ref}(R,l)|}},$$

where $|F_{ref}(R,l)|$ is the reference amplitude and $\delta\phi$ is the phase difference between the test and reference data at radius, R, along layer-line, l. An upper limit of 1·035 was allowed for the radial factor needed to provide consistent scaling of test with reference data (after correcting for magnification differences between the two). Trial maps calculated from tubes for which the factors exceeded this limit appeared to show poorer resolution in the radial direction, suggesting that they were unduly flattened.

The reassignment of layer-lines was done to place them in close-to-average positions in the diffraction pattern, and was according to the helical selection rule:

$$l = -81n + 253m \ (n = 2n'),$$

where m is an integer and n is the start number of the contributing helix. This selection rule gives numbers of 31 and 20, respectively, for the principal (1,0;−16) and (0,1;6) layer-lines; several of the tubes analysed were of this helical character (see Table 1).

The effects of the ctf in modulating the amplitudes of the layer-line peaks, and in reversing the signs of their phases, were taken into account in the merging. Each Fourier term from each image, $F_i(R,l)$, was multiplied by

the appropriate ctf value, $T_i(R,l)$, and the resultant corrected Fourier term, $F(R,l)$, was calculated as follows:

$$F(R,l) = \frac{\Sigma_i W_i(R,l) T_i(R,l) F_i(R,l)}{\Sigma_i W_i(R,l) T_i(R,l)^2},$$

where $W_i(R,l)$ is a weighting term associated with each image. This formula is similar to that given by Saxton (1978), for combining images that complement each other in terms of missing object information. Since the corrected Fourier terms are obtained by dividing by $\Sigma T_i(R,l)^2$, it is important in terms of signal to noise ratio to ensure that all spacings are well sampled. Defocus levels for the images were therefore chosen so that the ctf zeros would fall in a wide range of positions (Table 1; Fig. 2b).

There were 2 components to the image weighting term $W_i(R,l)$: one proportional to the length of the tube, and the other dependent on the quality of the data as a function of Z and R. A statistical assessment was made of each image dataset to determine the variable weighting component. The datasets were divided into Z and R sectors, and evaluated in each sector in annuli at successively higher resolution, using the absolute value of the parameter, $Q = \Sigma|F(R,l)|\cos\phi/\Sigma|F(R,l)|$ (ϕ is the phase angle, ideally 0° or 180°) as a measure of the quality of the data. With most images the quality was better along Z, whereas for a few images the R direction was the best. Two low-resolution and 2 high-resolution Q values were derived for each dataset (one along Z and the other along R) and the variable weighting component was calculated from these.

(f) *The equatorial layer-line*

The equatorial layer-line was not merged in the same way as the other layer-lines, because the terms on this layer-line extend to very low resolution and are influenced disproportionately by small irregularities in the image. Instead, the equators were examined individually. First, they were corrected by dividing by the appropriate ctf values, omitting Fourier terms near the ctf zeros. Then the corrected terms were converted, by a Fourier-Bessel inversion, into mean densities as a function of radius. With the weakly defocussed images, the signal to noise ratio at low resolution was poor, so the calculated density variations from the different images were inconsistent with one another. For 6 of the more strongly defocussed images, however, the calculated density variations were virtually identical, indicating 4 main peaks of density within an annulus of 210 to 385 Å, and approximately zero density outside (Toyoshima & Unwin, 1990). The corrected Fourier terms from these images were averaged and used as the equator for the merged dataset.

(g) *Calculation of the structure*

Separate criteria were used to fix the start and end points of each of the merged layer-lines. The start points were located 6 grid units inside the radius, R, of the first peak along the layer-line. The formula, $2\pi r_{max}R = 1{\cdot}03|n| + 1{\cdot}0$, was used to estimate R in relation to the maximum distance of density from the tube axis, r_{max}, and the Bessel order, n. (This formula is a slightly better approximation for high Bessel orders than that usually given, e.g. Moody, 1990.) The end points were made to be the points at which running Q values, calculated over a window width of 3 or 4 peaks, fell below 0·75 (a figure derived empirically from trial maps, using density fluctuations in the ice (radius <210 Å) as an indicator of signal to noise ratio).

Of the 287 possible layer-lines, 57 (mainly those for which $n>200$) were eliminated by applying these criteria. Those remaining (230) constituted the final dataset, and were incorporated in a Fourier-Bessel inversion to derive the helical density waves. Three-dimensional maps in sections parallel and perpendicular to the tube axis were then calculated by Fourier synthesis in the standard way (Klug *et al.*, 1958; DeRosier & Moore, 1970).

For 5-fold averaging of densities in the receptor structure, 5-fold centres of rotation were determined in planes parallel to the tube axis at several levels in the 3-dimensional map. The co-ordinates of each of the centres delineated the 5-fold rotation axis, which was found to lie along a radial line, i.e. exactly normal to the axis of the tube.

3. Results

(a) *The tubes*

Earlier work had investigated three helical families of tubes (Toyoshima & Unwin, 1990). These families were categorized in terms of the indices (−15,5), (−17,5) and (−16,6) to indicate the start numbers of the two principal helices in each case. The present work is concerned just with the (−16,6) family (Fig. 1a). Tubes of this family were found to have two advantages over the others for high-resolution data collection. First, they were wider (770 Å diameter, compared to 700 Å for the (−15,5) and 750 Å for the (−17,5) tubes), and consequently tended to be more rigid and straight. Second, pilot studies showed that overlap of Bessel terms along layer-lines, due to a particular orientation of the surface lattice with respect to the tube axis, occurred less frequently with this family than with the others.

The (−16,6) tubes are symmetrical structures, having an axial 2-fold rotation axis in addition to the four kinds of radial 2-fold axes generated by the p2 surface lattice (Fig. 1b).

(b) *Images*

Figure 3 shows some images of the tubes, typical of those selected. The images were recorded over a wide range of defocus (Table 1), so that the zeros of the contrast transfer functions (ctfs) would fall in a range of positions and that most spacings would be well sampled. Important features of the images were a constant diameter and straightness of the tubes, and the presence of high-resolution detail in all directions.

Previously, we used similar images, recorded in pairs, to obtain a 17 Å resolution structure (Toyoshima & Unwin, 1988*a*,1990). The second image was more strongly defocused than the first, and the defocus difference was such that by summing the two images out to the first zeros of their respective ctfs all spacings would contribute to the dataset with approximately equal weight. It was assumed that the additional radiation damage associated with the second image would not have a significant

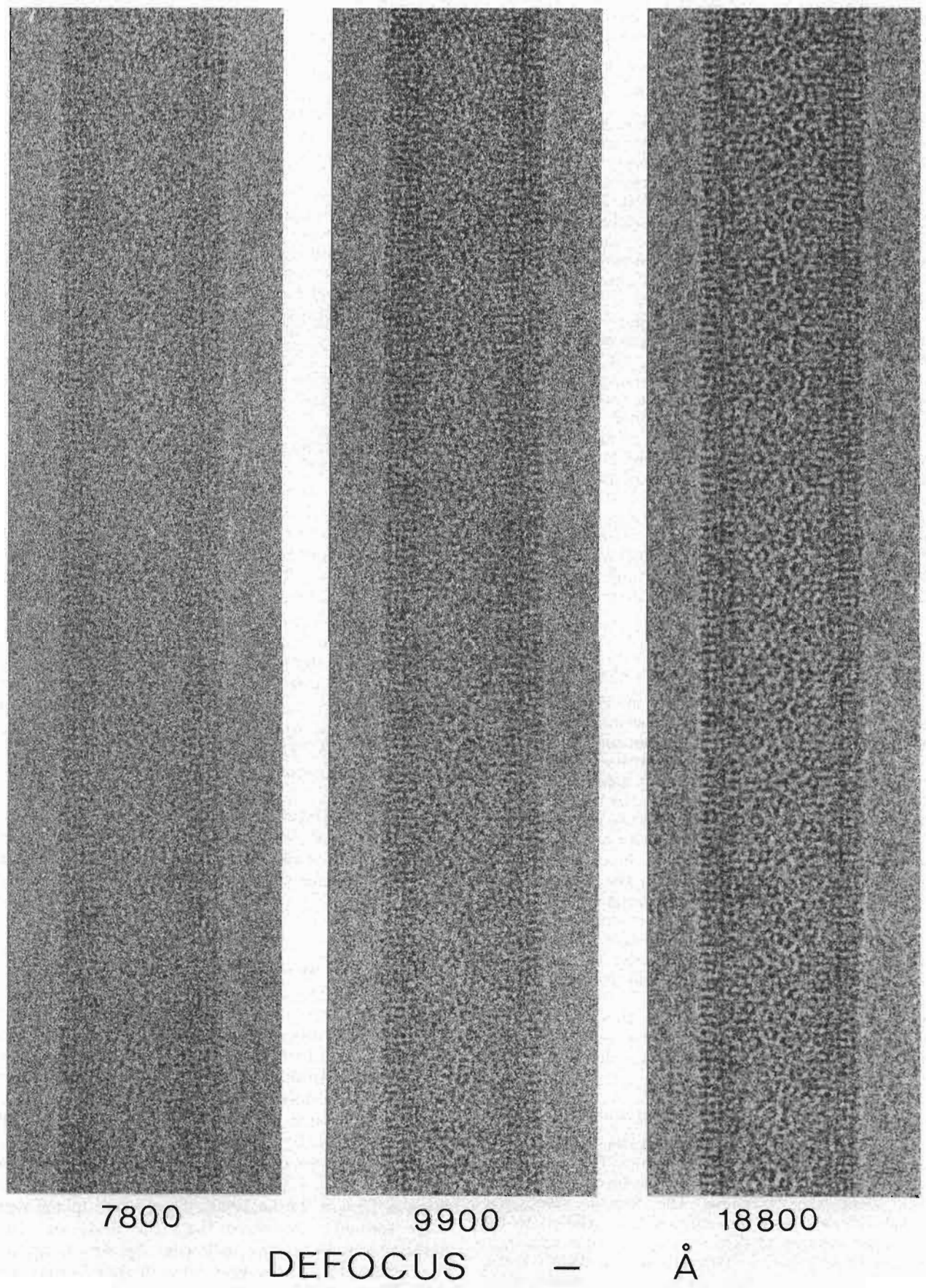

Figure 3. Images of (−16,6) tubes at different levels of underfocus. The tubes are embedded in amorphous ice over holes in the carbon support film. The gross features of the receptor are seen most clearly in the tube on the right, because of the enhancement of the low spatial frequency information when the image is a long way out of focus. The tube diameter corresponds to 770 Å.

Table 1
Details of individual images

Film no.	Defocus (Å)[a]	Layer-line assignments[b]	Ratio[c]	Repeat distance (Å)	No. of receptors[d]
613	7000	64,41	0·641	6063	2080
6437	7200	45,29	0·644	4334	2900
6728	7300	31,20	0·645	2988	2854
5279	7400	37,24	0·649	3513	1756
7321	7600	31,20	0·645	2958	1400
2381[e]	7600	23,15	0·652	2227	1528
1200[e]	7700	23,15	0·652	2219	1522
1704[e]	7800	14,9	0·642	1329	1530
1689[e]	8000	17,11	0·647	1630	1412
3390	8200	39,25	0·641	3659	1548
3009	8300	32,21	0·656	3079	1742
5301[e]	8300	23,15	0·652	2253	2320
3929	8800	38,25	0·658	3655	3606
2400	9400	43,28	0·651	4119	1413
989	9500	37,24	0·649	3603	2472
3141	9500	31,20	0·645	2971	1624
970	9900	45,29	0·644	4304	3660
959[e]	10,000	20,13	0·650	1931	1778
9879[e]	10,300	26,17	0·654	2124	1990
9612	10,400	31,20	0·645	2976	2042
880	11,000	43,28	0·651	4171	2704
1984[e]	12,400	20,13	0·650	1926	2496
143[f]	13,500	53,34	0·642	4931	2740
769	15,700	31,20	0·645	2907	1698
812	16,500	39,25	0·641	3625	1758
643	18,800	36,23	0·639	3393	2328

[a]All the figures denote levels of underfocus.
[b]For the principal (1,0;−16) and (0,1;6) layer-lines (see Fig. 4a).
[c]Ratios of heights of the principal layer-lines: (0,1;6)/(1,0;−16).
[d]Calculated from the (fractional) number of repeats analysed and the number, u, of the meridional layer-line at 1/11·6 Å^{-1}; number of receptors/repeat = $4u$.
[e]With these images some of the layer-lines overlap at high resolution and so only partial datasets have been collected (see Experimental).
[f]Image recorded at 200 kV.

effect on the quality of the data, since the strong low-resolution Fourier terms were not appreciably weakened by the low electron doses applied (Toyoshima & Unwin, 1988*b*). However, a further investigation of the effects of radiation damage, made in the course of the present work, showed that the ripples subsidiary to the strong terms, in the case of the second images, had poorer phases and were often much weaker (their amplitudes being reduced by a factor of up to about 2). Comparison between pairs of three-dimensional maps calculated from the pairs of images suggested that this degradation might be associated with displacement of material in the direction of the electron beam. Since such a distortion would adversely affect the quality of the information at high resolution, we used only the first images (doses < 8 electrons/Å^2) for this study.

(c) *Fourier transforms*

Fourier transforms computed from the images (Fig. 4a) consisted of a series of layer-lines lying perpendicular to the axis of the tube. The amplitudes along these layer-lines were modulated by the ctf, which is seen in Figure 4b as a series of weakly visible concentric rings. With individual images, the signal to noise ratio was not good enough for layer-lines to be distinguished above background beyond a resolution of about 20 Å. The higher resolution layer-lines did however appear after the data were merged, so that the noise was averaged out (Fig. 4c).

Each image was evaluated to see how the quality of the Fourier terms varied as a function of axial spacing (Z) and radius (R). A quadrant of its transform was split equally into Z and R sectors, and Q values (see Experimental, section (e)) were determined in annuli at successively higher resolution. The quality of the data, assessed in this way, was generally good in both directions at low resolution (spacings larger than 17 Å), but was poor beyond this (Table 2), reflecting the fact that the high-resolution terms from single images were very weak.

(d) *Combined data*

Altogether 26 images (each typically containing 2000 receptors) were used to obtain the combined dataset. Table 1 gives some details. The images were different from one another in terms of the exact

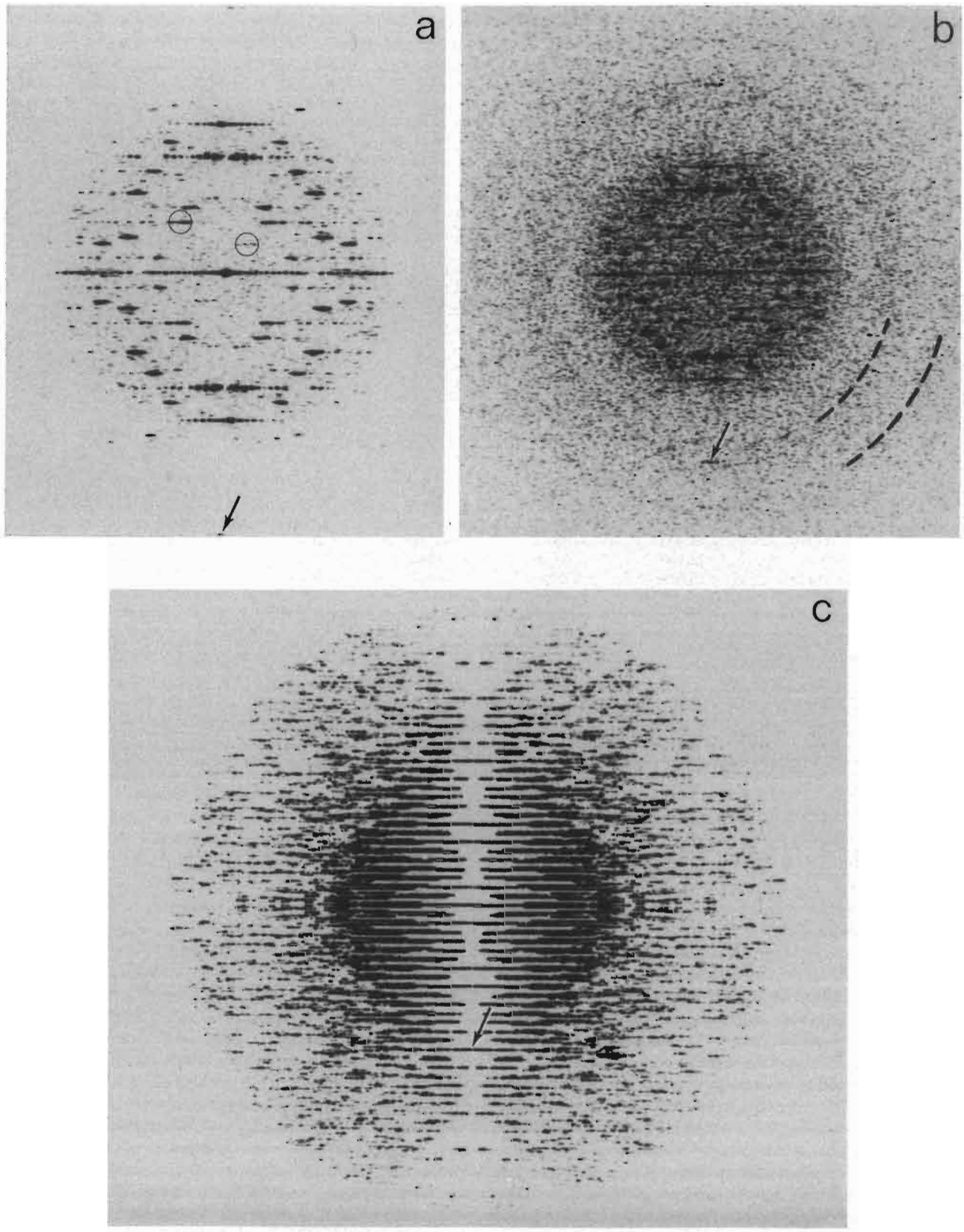

Figure 4. Fourier transform of an image of a tube (film 769) weakly exposed (a) to show the layer-line pattern, and (b) strongly exposed to show the superimposed modulations associated with the ctf. These modulations consist of a series of concentric rings (broken lines), only 2 of which are directly visible in b because of the small area transformed. The modulations are much clearer, and can be seen to extend to higher resolution, after rotational averaging (Fig. 2a), allowing a defocus value of 15,700 Å to be estimated for the image. c, A Fourier transform calculated for the (−16,6) tube after merging the data from 26 images. Many more layer-lines having phases close to the ideal values can be seen than in Fourier transforms from individual images, because of the improvement in signal to noise ratio as a result of averaging; the Fourier transform extends to a resolution of 8·7 Å. In a the principal (1,0; −16) and (0,1;6) layer-lines (from one side of the tube) are encircled. The position of the (2,4; −8) layer-line (arrow in a, b and c) corresponds to a resolution of 20·8 Å. This layer-line appears to lie on the Z-axis (meridian) in a and b because the tube is slightly tilted (2°) away from the plane normal to the electron beam.

Table 2
Statistics of Fourier transforms

Resolution range (Å)	*Z*-sector		*R*-sector	
	$\|F_{avg}\|$[a]	Q[a]	$\|F_{avg}\|$	Q
A. *Single image (film 769)*				
68·0–34·5	155·4	0·89	137·1	0·84
34·5–22·8	115·8	0·76	70·8	0·76
22·8–17·0	30·4	0·75	28·7	0·75
17·0–13·7	20·6	0·65	22·1	0·63
13·7–11·4	17·1	0·70	19·6	0·65
11·4–9·8	15·1	0·65	17·5	0·58
9·8–8·7	14·0	0·56	15·4	0·61
B. *Combined data*				
68·0–34·5	244·8	0·97	217·3	0·97
34·5–22·8	106·5	0·82	63·2	0·87
22·8–17·0	38·2	0·75	18·9	0·80
17·0–13·7	14·6	0·75	8·6	0·66
13·7–11·4	8·7	0·76	6·6	0·69
11·4–9·8	5·9	0·66	5·6	0·71
9·8–8·7	3·6	0·75	3·2	0·64

[a]Average amplitudes and Q values (see Experimental, section (e)) taken from the strongest 50 peaks in each resolution range.

Table 3
Summary of three-dimensional data

Number of images	26
Number of layer-lines	230
Number of Fourier terms	9123
Maximum Bessel order	220
Two-fold phase residual (deg.)	10·6
Resolution cut-off (Å)	8·7

geometry of the p2 surface lattice. Because of the disparities, the helical repeat distance varied by a large amount (between 1329 and 6063 Å), leading to a range of assignments (layer-line numbers) for the two principal (1,0;-16) and (0,1;6) layer-lines. However, the ratio of heights of these layer-lines ($0{\cdot}647 \pm 0.005$ S.D.), and the dimensions of the p2 surface lattice calculated from them ($a = 80{\cdot}2(\pm 0{\cdot}3)$ Å, $b = 145{\cdot}5(\pm 0{\cdot}6)$ Å, $\gamma = 114{\cdot}0(\pm 0{\cdot}5)°$; at 290 Å radius), did not vary by more than 1%. Such variations were insignificant in relation to the resolution achieved and therefore did not have to be taken into account.

The Fourier transform obtained by merging all the images consisted of 9123 terms (Fig. 4c), and yielded an amplitude-weighted 2-fold phase residual (comparing individual phases with their nearest centrosymmetric values) of 10·6°. The higher resolution terms in this transform (17·0 to 8·7 Å) were weaker than those in the individual transforms, but their quality in both the *Z* and the *R* sectors had improved (Table 2). This improvement was more marked in the *Z* sector, possibly reflecting the fact that the *Z*-sector annuli contain a higher proportion of peaks of low-order Bessel order (which tend to be stronger), rather than that the data along the *R* direction are inherently poorer.

The phase and amplitude variations along some of the (230) layer-lines are plotted in Figure 5. Many layer-lines consisted of a group of several strong peaks, as expected from the wide (210 to 385 Å) radial distribution of densities, followed by a series of weaker subsidiary peaks. In general, the phases of all the strong peaks and most of the subsidiary peaks were close to the ideal values (0° or 180°). Layer-lines for which the Bessel orders were greater than about 200 were very weak and did not show such good agreement with the ideal values, but most of these layer-lines had been eliminated from the final dataset (see Experimental, section (g)).

A summary of the combined data is given in Table 3.

(e) *Three-dimensional map*

Figure 6 shows a cross-section of the tube, calculated from the combined Fourier terms. It cuts through several receptors and depicts one of them in profile. The other components visible are the phospholipid headgroups of the bilayer (shaded) and a separate mass of protein, which is attached to the receptor at its (cytoplasmic) base.

An important feature in Figure 6 is the cation-conducting pathway (long arrow), which passes centrally down the axis of the receptor and would, in the open conformation, make a continuous aqueous link across the bilayer to the regions on either side. This pathway consists of three parts: in the synaptic portion, extending to the outer radius of the tube, it forms a water-filled opening about 20 Å in diameter and 60 Å long (the synaptic entrance to the pore); in the cytoplasmic portion, it forms a second 20 Å diameter opening, which is about 20 Å long (the cytoplasmic entrance to the pore); across the lipid bilayer, it forms a more constricted region about 30 Å long (the pore). The pore narrows less rapidly from the synaptic than the cytoplasmic side, and near the middle of the bilayer becomes so constricted that the density within it is as high as in other parts of the molecule. Evidently, it is this region of the closed channel where the pathway is blocked.

The protein mass underlying the cytoplasmic entrance is not seen in tubes frozen in high pH solution and so was proposed to be part of the 43K protein (Toyoshima & Unwin, 1988*a*), which binds to the *Torpedo* receptor in near-stoichiometric amounts (LaRochelle & Froehner, 1986). Only parts of these molecules would have been seen if they were not arranged regularly on the same surface lattice as the receptor. At the higher resolution of the present study, the densities corresponding to this mass are more clearly separated from the densities associated with the five subunits of the receptor. They also appear to be divided into two roughly equal parts, suggesting that the mass could in fact be composed of equivalent portions of two molecules linking together underneath the channel.

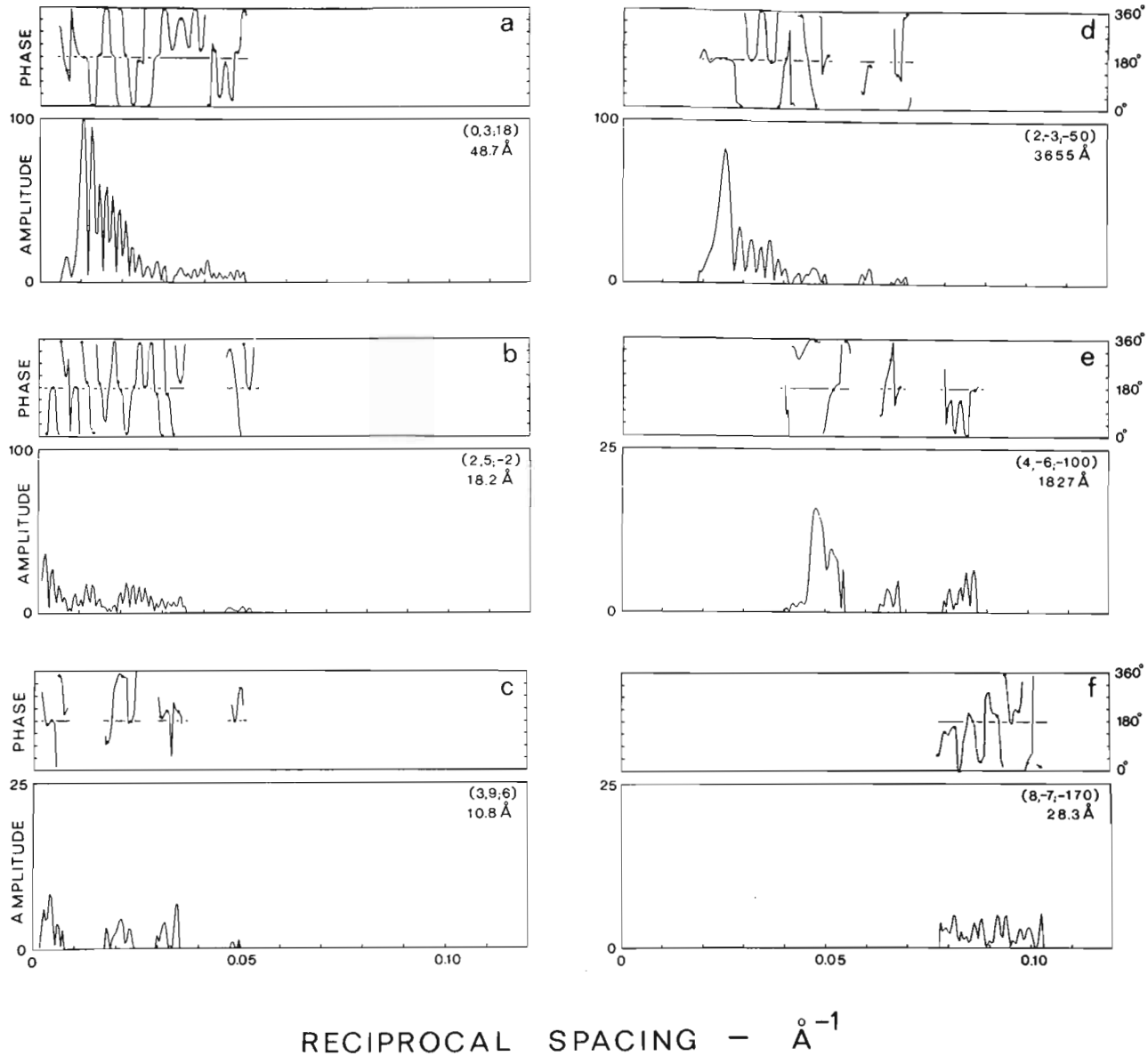

Figure 5. Examples of phase and amplitude variations along typical merged layer-lines, covering a range of resolutions (a to c) and Bessel orders (d to f). The layer-lines are identified by their $(h,k;n)$ indices (Toyoshima & Unwin, 1990), and their axial resolutions (along Z). Most peaks in the amplitude plots (lower panels) are associated with phases (upper panels) that are close to the ideal values of 0° or 180°. The strong, low-resolution layer-lines have almost negligible departures from centrosymmetric phases (data not shown).

(f) *Structure of the receptor*

The overall surface appearance of the receptor (Fig. 7) resembles that described previously (Toyoshima & Unwin, 1990) although, at the higher resolution, the distinction between the (irregular) water-facing and (smoother) lipid-facing surfaces is more obvious. The lateral dimensions are greatest about half-way up the synaptic part of the molecule, and neighbouring receptors pack tightly together in this region. As discussed later, the rather complex appearance of the surface here may reflect a specialized underlying structure that, in the α subunits, is involved in shaping the acetylcholine binding pocket. The receptor fits within a cylinder 80 Å in diameter and 125 Å long, with about 55% of its mass on the synaptic side of the phospholipid headgroups, and 20% on the cytoplasmic side. The synaptic portion extends about 60 Å above the headgroups, and the cytoplasmic portion extends about 20 Å below them, such that the tip of each subunit touches, or comes very close to the 43K protein at the base.

The internal structure of the receptor, at two levels, contains distinct rods of density that are oriented predominantly perpendicular to the bilayer; the rods lie in approximate 5-fold positions and pack against each other with spacings typical of α-helices. In the synaptic part, about 30 Å above the bilayer surface (region SS′ in Fig. 6), there is a

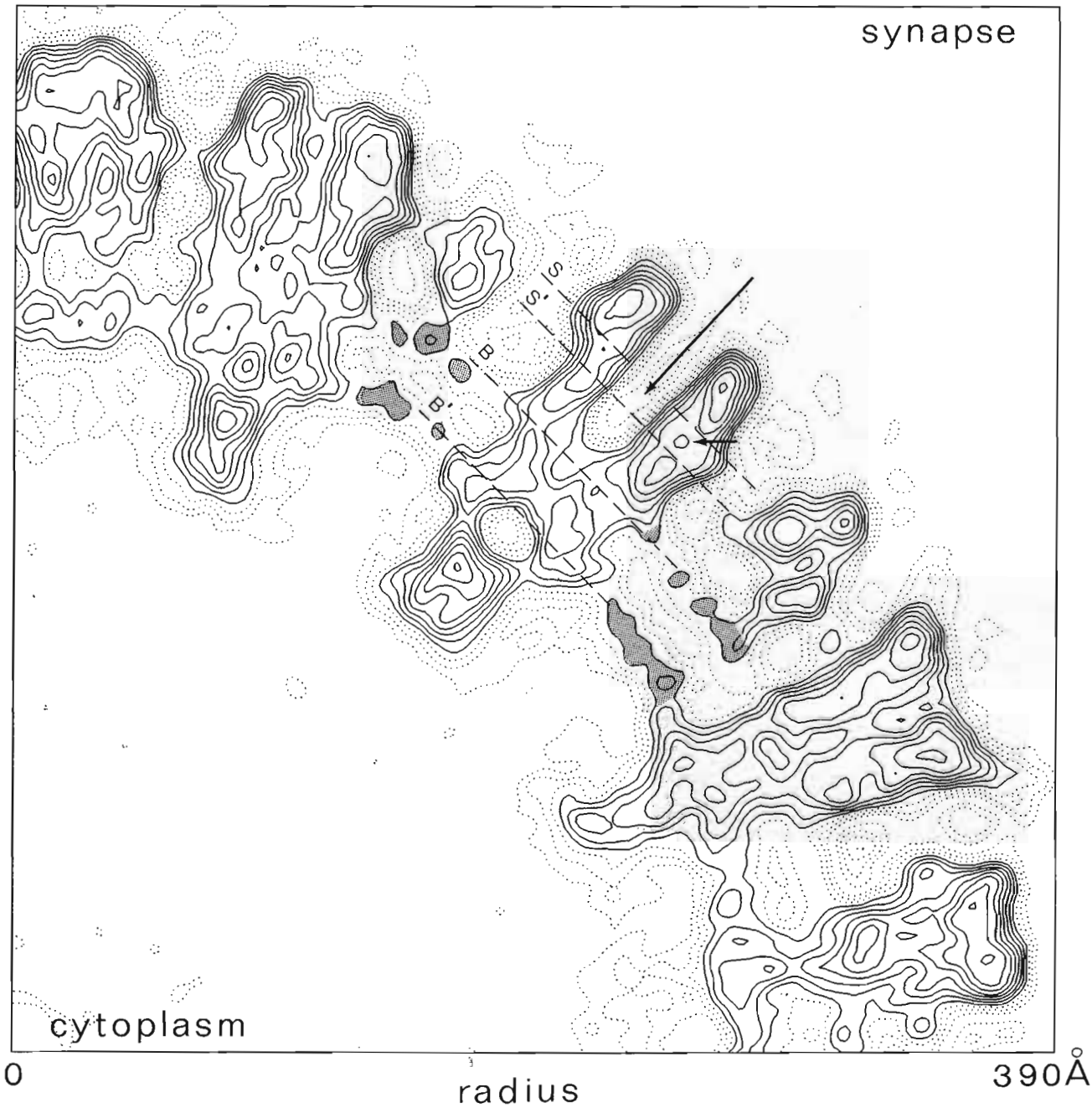

Figure 6. Cross-section of the tube showing a receptor in profile, the surrounding headgroups of the lipid bilayer (shaded) and the attached (43K) protein at its (cytoplasmic) base. The long arrow indicates the path taken by the ions along the central axis of the receptor; the short arrow points to a specialized region of the receptor, 30 Å above the bilayer surface which, in the α subunits, may be where the acetylcholine binds (see the text). Slabs through the 3-dimensional map extending over the portions, SS′ and BB′ are shown in Figs 9 and 11. The tube axis is in the bottom left-hand corner. The continuous contours indicate densities greater than that of water; the lowest contour has been omitted.

group of three rods in each subunit. In the bilayer-spanning region (region BB′ in Fig. 6), there is another arrangement of rods, closer to the 5-fold axis and involving only one rod in each subunit, rather than three.

(g) *Synaptic rods*

The groups of three rods, located in each subunit about 30 Å above the bilayer surface, give rise to three peaks of density in cross-sectional views (Fig. 8). The two closest together peaks (centre to centre spacing 11 Å) lie next to the entrance of the channel and the third lies on the outside. As would be expected, equivalent peaks in the two α subunits look similar. Of the other subunits, that lying between the α subunits seems to resemble the α subunits the most, and so (in this region) may have the closest sequence homology. The three rods together create an apparent cavity near the centre

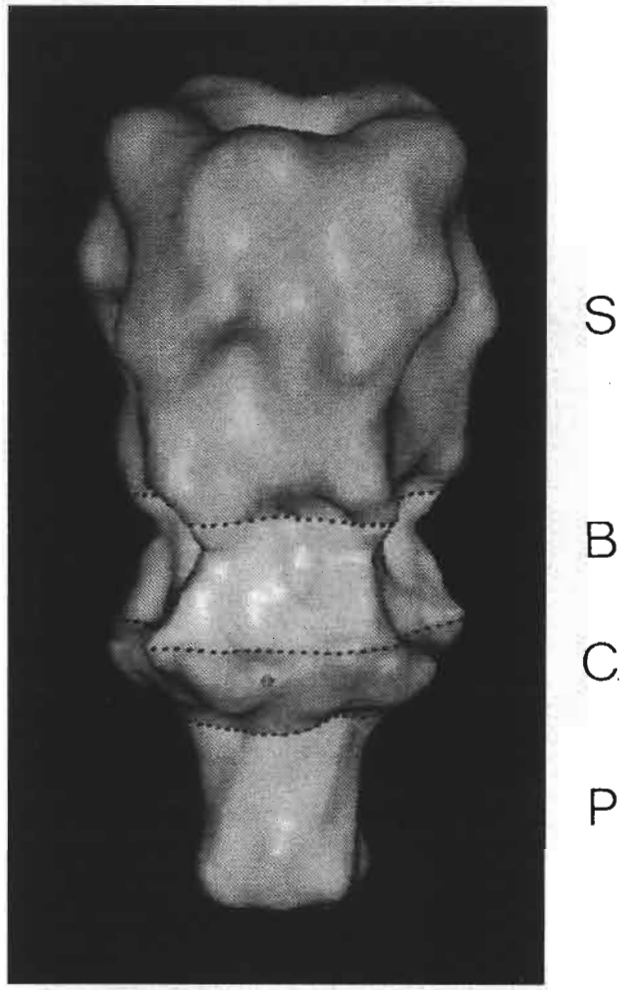

Figure 7. Model of the receptor, and attached protein (P, bottom), showing the overall surface appearance. The band across the receptor (B) corresponds to the hydrophobic core of the bilayer, and separates the large synaptic mass (S, above) from the smaller cytoplasmic mass (C, below). The receptor has been 5-fold averaged to emphasise the surface features common to each subunit, and displayed using the program, SYNU (Hessler *et al.*, 1992), at a density cut-off level chosen to include 80% of its molecular mass (290 kDa).

of each subunit, and a bulge on the outer subunit surface. The internal cavity is visible in the profile view of the receptor (small arrow, Fig. 6).

In the α subunits, the cavities are most pronounced and may be water-filled, since the densities at their centres are particularly low: lower, for example, than the density in the pore in the region where it is most constricted. The cavities of the α subunits are also associated with a hollowed-out region on the surface (arrows in Fig. 8). This same feature is evident at lower resolution (Toyoshima & Unwin, 1990; Fig. 11b), and is less well developed or absent in the other subunits.

Figure 9 is a slab through one of the α subunits, which illustrates how the rods pack in three dimensions. They twist around each other, making a left-handed coil. The rod lining the entrance to the channel on the left in this Figure is very short (accounting for the weaker densities). The outer rod is longer than the other two, and may extend down to the bilayer surface. The cavity is made by the outer rod tilting radially outwards.

(h) *Pseudo-5-fold symmetry*

While the individual subunits have many features in common, and the two equivalent subunits (the α subunits) are similar throughout the entire structure, the densities are not yet accurate enough to make it possible to account for minor differences between subunits in an unambiguous way. For the present purposes, it is noted that the internal features of the individual subunits (Figs 8 and 10, left-hand panels) are arranged in approximate 5-fold positions (within about 2 Å), and that therefore a good estimate of the structure common to all subunits is obtained by 5-fold averaging. Figure 10 gives examples of sections through the bilayer-spanning region of the receptor before and after 5-fold averaging. The symmetrized map is used to describe the bilayer-spanning structure, since no distinction can be made between individual subunits in this part of the receptor.

Figure 8. Section normal to the pseudo-5-fold axis of a single receptor, 30 Å above the bilayer surface (tube radius, 338 Å). The contours extend out to the estimated surface of the receptor; the cut-off level for the continuous contours has been chosen to highlight the density peaks composing each subunit. There are 3 density peaks in each subunit, arising from 3 rods running approximately normal to the plane of the section (Fig. 9). The labels and the star indicate respectively the positions of the 2 α subunits and the α-bungarotoxin binding sites, according to low-resolution studies of the receptor in projection (Kubalek *et al.*, 1987). The arrows point to clefts, which are distinctive features of the α subunits. The horizontal dimension of the section corresponds to 108 Å.

Figure 9. Detail associated with the α_1 subunit in the region 30 Å above the bilayer surface. The 3-dimensional contour map is a 12 Å thick slab extending over the portion, SS′, in Fig. 6. It is made by stacking sections normal to the pseudo-5-fold axis (bottom) on top of each other, and is viewed from above. The contours extend out to the estimated surface of the receptor; the continuous contours and shaded discs highlight the paths taken by the 3 rods around a central cavity. The dotted line lies along a cleft connecting the outer surface to the cavity. The cleft appears to be shaped partly by a neighbouring subunit (δ subunit; Kubalek *et al.*, 1987). The length of the dotted line corresponds to 20 Å. The interval between sections corresponds to 2 Å.

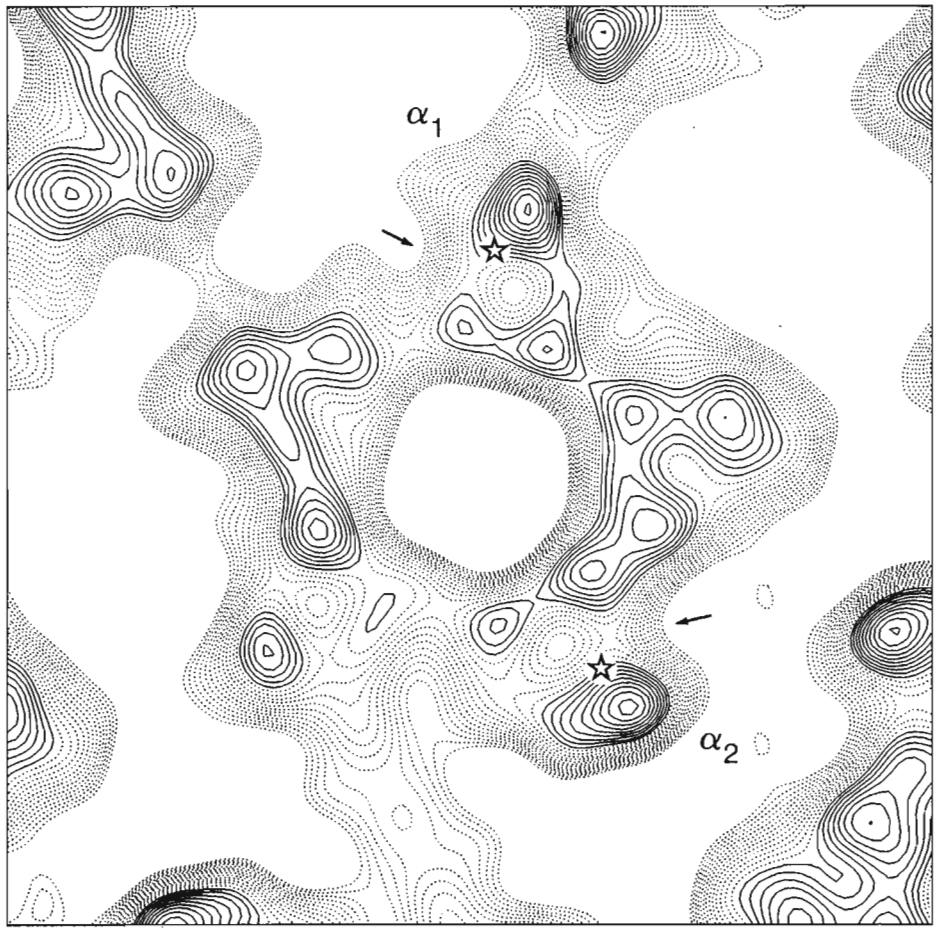

Fig. 8.

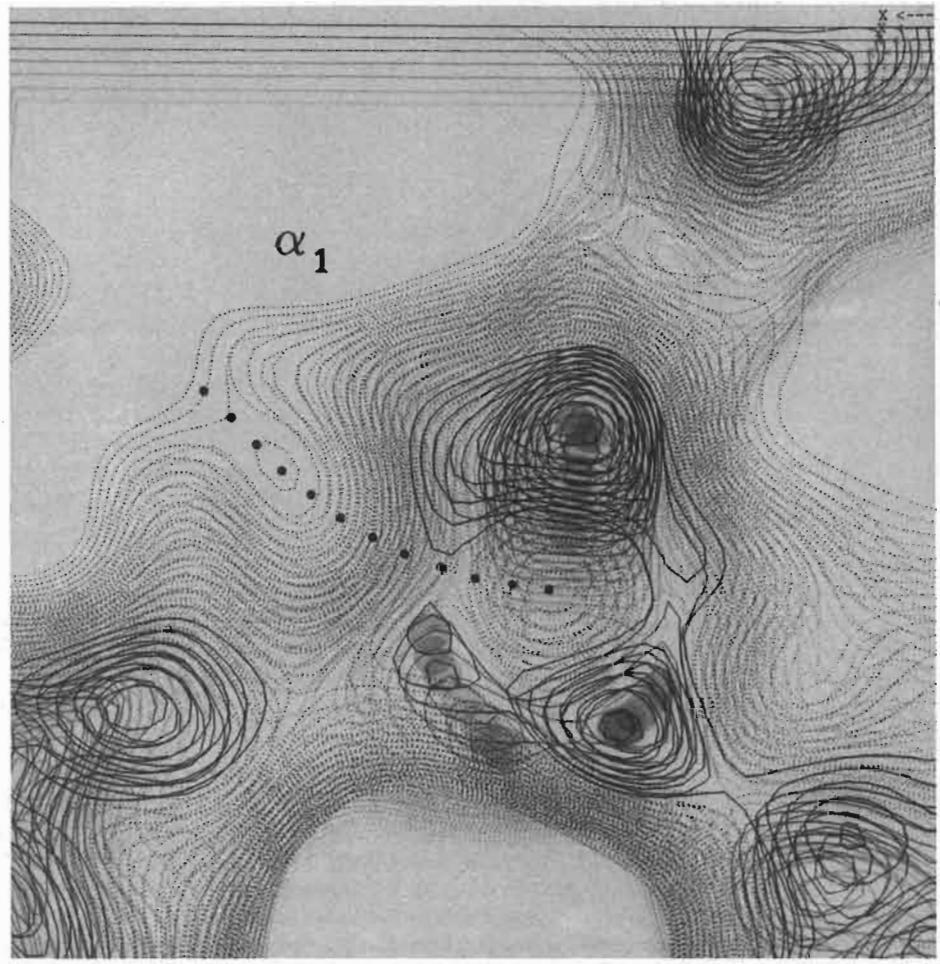

Fig. 9.

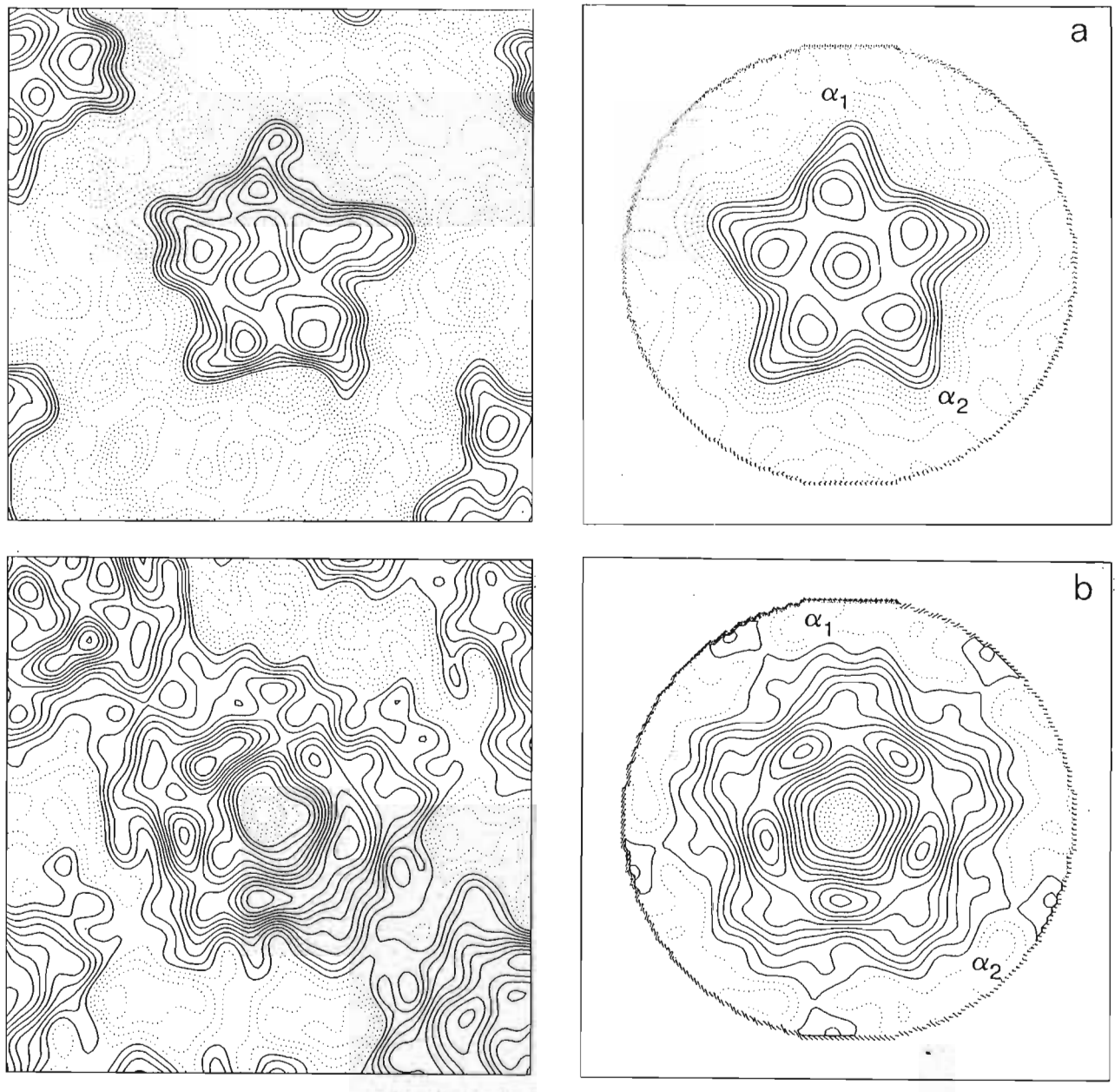

Figure 10. Sections normal to the pseudo-5-fold axis of a single receptor, in the bilayer-spanning region, before (left) and after (right) 5-fold averaging. The sections are at levels corresponding to (a) the middle of the synaptic leaflet of the bilayer (tube radius, 294 Å), and (b) the cytoplasmic leaflet of the bilayer at the phospholipid headgroups (tube radius, 276 Å). The cut-off level of the continuous contours has been chosen so that the total mass included by all the sections corresponds to the molecular mass of the receptor. The horizontal dimension of each section corresponds to 108 Å.

(i) *Bilayer-spanning region*

As mentioned above, only one rod is visible in each subunit where it traverses the bilayer. In sections through the bilayer before 5-fold averaging (Fig. 10, left), there are no other convincing peaks of density in any of the subunits that could correspond to other rods. The five observed rods together form a ring lining the pore, and are therefore interpreted below as corresponding to the M2 segment of the sequence.

Lying outside these rods is additional density that appears to form a continuous rim around them. This rim is thinnest in the synaptic leaflet of the bilayer (Fig. 10a), where it restricts the cross-section of the receptor to only 380Å^2/subunit. The rim thickens near the cytoplasmic phospholipid headgroups (Fig. 10b), and extends into the cytoplasm to create the substantial mass forming the cytoplasmic entrance of the channel.

Figure 11 illustrates the three-dimensional appearance of the rim and the rods. The rim creates quite a pronounced bulge extending almost radially out from the rods (Fig. 11a). The rods themselves bend in passing through the bilayer, and therefore are best visualized after the upper and lower halves

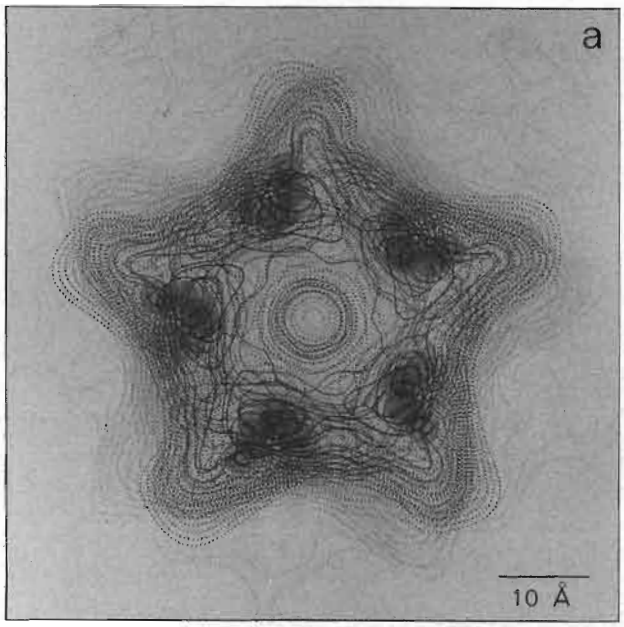

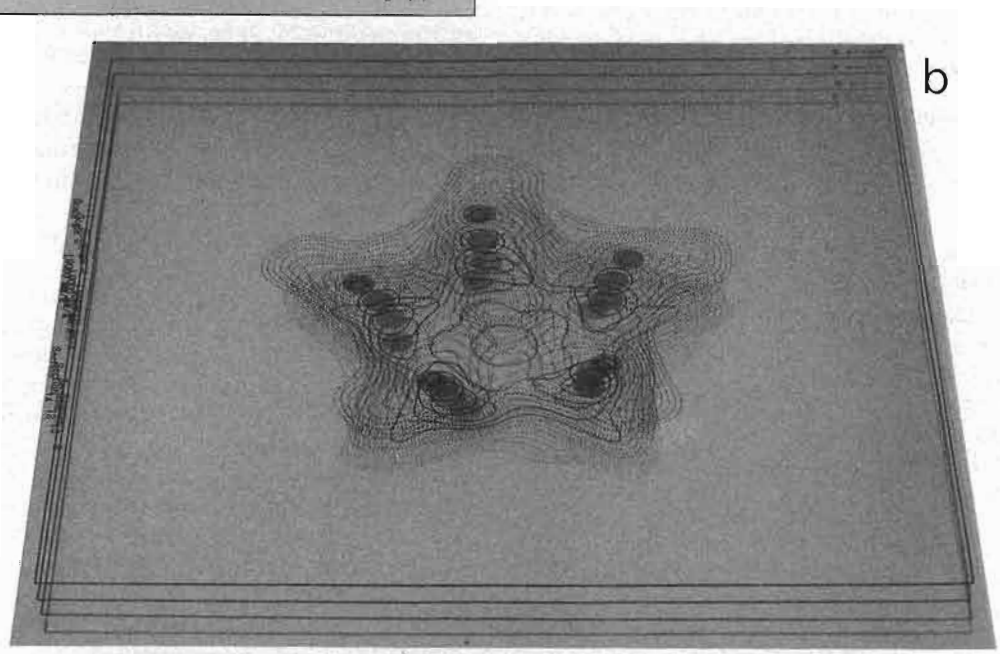

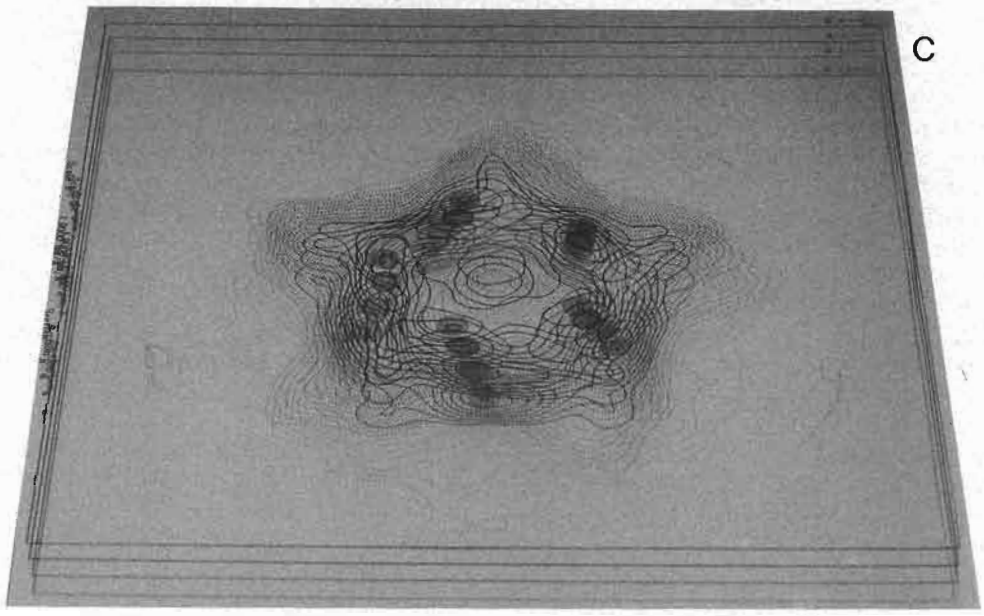

Figure 11. Three-dimensional contour map of the bilayer-spanning region of the receptor (a), and of the portions above (b) and below (c) the part where it comes closest to the axis of the pore. The views are from the synaptic side and extend over the portion, BB′, in Fig. 6. The bottom section in b and the top section in c are the same. The contours extend out to the estimated surface of the receptor; the cut-off level for the continuous contours has been chosen to highlight the paths taken by the peak densities (shaded discs) composing the rods lining the pore. The whole molecule has been rotationally averaged about the pseudo-5-fold axis (see the text) so that all subunits appear equivalent. The interval between sections in a and b corresponds to 4 Å; the horizontal dimension corresponds to 108 Å.

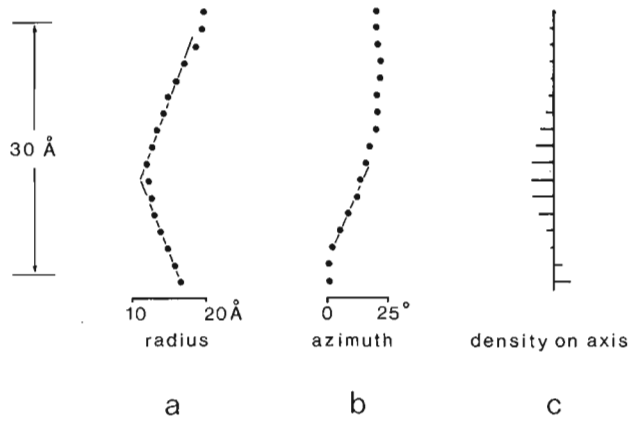

Figure 12. Details associated with the rods in the 30 Å wide region spanning the lipid bilayer (synaptic end uppermost), measured from 2 Å spaced sections through the 5-fold averaged structure. a, Radial distance of the peaks of density from the axis of the pore; b, azimuths of the peaks about this axis; c, density variation along the axis of the pore; bars to the left and to the right of the mid-line correspond to densities closer to that of protein and of water, respectively. Straight lines drawn through the points in a and b relate to features that are correlated with the amino acid sequence of M2 (Fig. 13b; see the text).

of the map have been split (Fig. 11b and c). It can be seen that the rods are most distant from the axis of the pore in the two headgroup regions, and come closest to the axis just below the middle of the bilayer (on the cytoplasmic side).

The shape of the rods changes across the bilayer. They have an approximately circular cross-section in the synaptic leaflet (Figs 10a and 11b), but the densities fall off more rapidly towards the pore, giving them a more elliptical cross-section, in the cytoplasmic leaflet (Figs 10b and 11c). The transition from a circular to an elliptical cross-section begins at a point near the middle of the bilayer.

(j) *Details of the transmembrane rods*

Measurements made from the map allow a more quantitative description of some aspects of these rods. Figure 12a plots their radial distance from the axis of the pore, estimated from the peaks of density in sections parallel to the bilayer surface. Their centres lie about 17 Å from the axis in the headgroup regions and come much closer than this at the apex of the bend, where the measurements are unlikely to be accurate because of the limited resolution. The apparent tilt of the rods away from the axis is about 23° above, and 25° below the bend.

Figure 12b shows that the altered appearance of the rods in the cytoplasmic leaflet is associated with some slewing of the densities around the pore. The rods also create a more open pore at the cytoplasmic headgroups than they do in the corresponding region on the synaptic side (Fig. 12c).

These features in the cytoplasmic leaflet seem to reflect a changing distribution of the mass composing the rods. Smaller side-chains on the face exposed to the lumen of the pore, than on the other faces, would account for the less circular cross-sections of the rods and the openness of the pore at the cytoplasmic headgroups (see Discussion, section (e)).

4. Discussion

The structure of the receptor at 17 Å resolution, determined earlier from several images of three different families of ice-embedded tubes (Toyoshima & Unwin, 1988*a*, 1990), revealed the rather complex nature of the outside surface of the receptor, the paths taken by the centres of mass of the subunits, and the contacts, involving the α and δ subunits, made by each receptor with its neighbours. The receptor was found to be about 120 Å long, and pseudo-5-fold symmetry was evident throughout its length. The cation-conducting pathway, delineated by the symmetry axis, was found to be partitioned into a narrow pore spanning the lipid bilayer, bracketed by wide cylindrical entrances on either side. This overall three-dimensional design was quite different in a number of respects from that obtained with negatively stained flattened tubes (Mitra *et al.*, 1989), possibly reflecting the fact that the frozen aqueous environment maintained better the state of the structure as it is in solution.

In the present study, the resolution has been extended to 9 Å by an analysis of just one helical family of tube (the (−16,6) family) and by merging data from many images, after correcting for the effects of defocus. The new map confirms the details found earlier, with the frozen tubes. In addition, it now resolves some internal features of the protein subunits corresponding to elements of secondary structure, and provides a clearer picture of the pore. These aspects are discussed below.

(a) *Secondary structure*

There are two groupings of rods, at equivalent 5-fold positions in the whole molecule, and oriented predominantly parallel to the long axes of the subunits. One of the groupings is in the part of the receptor extending into the synapse (Fig. 9), and the other in the part crossing the lipid bilayer (Fig. 11). It is assumed that the rods are α-helices from their dimensions, the way they pack and the way they twist around each other in the synaptic part of the structure. However, much of the protein interior is relatively featureless, suggesting that a large proportion of the polypeptide chain is in an extended or (unresolved) β-sheet configuration. The observed details support the circular dichroism measurements suggesting that α-helices make up about a quarter of the total mass (Mielke & Wallace, 1988). There is no evidence for the presence of 80 Å long α-helices, suggested by an interpretation of the X-ray diffraction pattern of partially oriented membrane samples (Ross *et al.*, 1977; Kistler *et al.*, 1982).

(b) *Putative acetylcholine binding pocket*

In the synaptic part of the receptor, about 30 Å above the bilayer surface, each subunit appears to contain a cavity surrounded by three α-helices (Figs 6, 8 and 9). Two of the α-helices also line the entrance to the channel. The third, which is tilted radially outwards to make the cavity, lies on the outside.

The α subunits are distinct from the other subunits in this region in two ways. First, their cavities are more open and, from their low densities, probably exposed to the aqueous surroundings. Second, they have a more pronounced hollow or "cleft" directed towards the cavity (arrow in Fig. 8; Toyoshima & Unwin, 1990; Fig. 11b). The cavities and clefts are in the vicinity of the two α-bungarotoxin binding sites, determined from labelling studies of receptors in projection (stars in Fig. 8; Kubalek *et al.*, 1987).

α-Bungarotoxin is a small (8 kDa) competitive antagonist that binds to the receptor at sites that overlap the binding sites for acetylcholine. It is possible, therefore, that the cleft in the α subunit represents the area of access for the acetylcholine molecule and that the cavity is the binding pocket. In this case the design would be something like that of the acetylcholine binding region in acetylcholinesterase, where there is a "gorge", about 20 Å long, which penetrates halfway into the enzyme and widens out close to its base (Sussman *et al.*, 1991).

The centre to centre distance between the two cavities in the α subunits is 42 Å. This distance, combined with the distance of 30 Å from the membrane surface, are within about 5 Å of estimates for the acetylcholine binding site locations, based on fluorescence lifetime and energy transfer measurements, using agonist and non-competitive inhibitor site probes (Herz *et al.*, 1989). The surroundings of the pocket seem also to account for the results of photoaffinity labelling studies (Dennis *et al.*, 1986,1988; Galzi *et al.*, 1990), indicating that the binding site is made up from three separate regions of the sequence, since these regions would be on the α-helices and/or at their ends. The pockets do not lie at the interfaces between subunits (Pedersen & Cohen, 1990), although the cleft of the α_1 subunit (Fig. 9) seems to be shaped partly by a neighbouring subunit. Differences between the α subunits in this region could be responsible for the finding that competitive antagonists such as α-tubocurarine bind to the two agonist recognition sites with different affinities (Neubig & Cohen, 1979).

(c) *Transmembrane folding*

The map inside the lipid bilayer reveals only one α-helix in each subunit, which is lining the pore (Figs 10 and 11). The single α-helical segment is surprising, given that hydropathy plots predict four. It is unlikely that the other α-helical segments are not resolved because the structure is disordered in the regions where they would be located. If this were the case, the minimum cross-section of the structure within the bilayer should be greater than the measured value of 380Å^2/subunit, and one would expect to find indications of at least some additional α-helices before 5-fold averaging (Fig. 10, left).

On the other hand, the helix that is observed is flanked on its lipid-facing sides by a continuous rim of density (Fig. 11a), and there could be several crossings of the polypeptide chain in the β-sheet configuration composing this rim. A single thickness of β-sheet (e.g. 5 or 7 strands, depending on the angle to the bilayer surface) would account for the densities. The topology then could still be consistent with the evidence that both the C and N termini are on the synaptic side, and that the links between M1 and M2 and between M3 and M4 extend into the cytoplasm (for a review, see Karlin, 1991).

The centre to centre spacing between neighbouring helices around the ring increases from about 12 Å in the middle of the bilayer to about 20 Å at the surfaces. The wide separation nearer the surfaces is not consistent with close helix to helix packing (Chothia, 1984), but could be achieved if the helices are lying on a framework of β-sheet. Such an organization would account for the labelling of the N-terminal end of M1 of the α subunit by the open channel blocker quinacrine azide (DiPaola *et al.*, 1990), since side-chains from the framework strands could contribute to the wall lining the pore in its wider parts. The wide separation of the helices might also account for the fact that a large proportion of the M2 residues appear to be exposed to the pore, when probed by cysteine-substitution mutants (Akabas *et al.*, 1992).

Interestingly, the appearance of the structure in (and just below) the bilayer-spanning portion of the receptor resembles that of two pentameric toxin complexes, each consisting of a ring of five α-helices surrounded mainly by β-sheet, whose atomic structures have recently been solved (Sixma *et al.*, 1991; Stein *et al.*, 1992). The densities over most of the bilayer (Fig. 11a) seem to correspond closely to those of the verotoxin-1 B pentamer (Stein *et al.*, 1992), where the β-sheet structure bulges out almost radially from each of the helices in the ring. The densities at the bottom of the bilayer-spanning portion (Fig. 10b) look more like those of the B subunit pentamer of enterotoxin from *Escherichia coli* (Sixma *et al.*, 1991), where the mass outside the helices is more uniformly distributed. These resemblances must be partly superficial, since the toxins are soluble proteins. However, the segments, M1, M3 or M4, of the receptor subunits may form sets of three anti-parallel β-strands, analogous to those present in both toxins. Also, the interactions between the receptor subunits would presumably entail hydrogen bonding between the main-chain backbone groups of the β-sheet segments, as with the toxins. This would allow a continuous ring of β-sheet, a barrel, to be created, which would be a stable configuration in the hydrophobic surroundings (Weiss *et al.*, 1991; Cowan *et al.*, 1992).

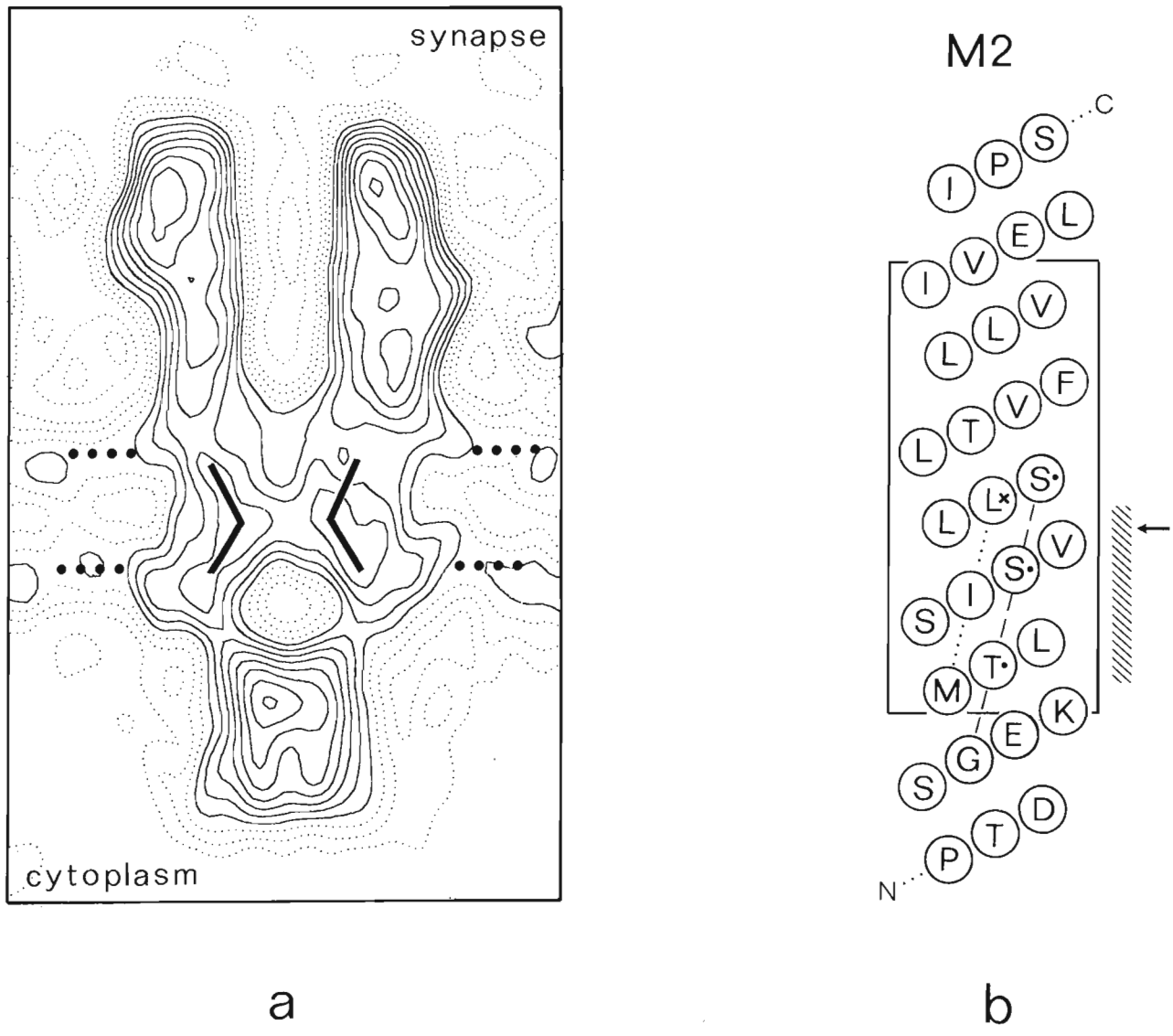

Figure 13. a, Channel in profile with positions of the transmembrane rods (Fig. 12) and estimated limits of the lipid bilayer (dotted lines, 30 Å apart) superimposed. b, Helical net plot of the amino acid sequence around M2 (*Torpedo* α subunit). The broken line identifies a face on the helix composed entirely of small residues. This face, flanked by bulky hydrophobic side-chains (dotted line), confers on the helix a distinctive shape, facilitating alignment of the densities in the 3-dimensional map (see the text). The shaded bar indicates the estimated location of the line in Fig. 12b, and the arrow is at the estimated location of the "kink" (Fig. 12a); hence, the bilayer-spanning segment is the stretch included in the rectangle. The cross denotes the conserved leucine residue, Leu251; the dots denote other residues that, when mutated, affect binding of QX-222 (Leonard *et al.*, 1988; Charnet *et al.*, 1990) and (lowest dot) ion flow through the pore (Villarroel *et al.*, 1991; Villarroel & Sakmann, 1992).

(d) *The M2 helix*

The rod spanning the bilayer forms the wall lining the pore and should therefore correspond to the M2 helix (Giraudat *et al.*, 1986; Hucho *et al.*, 1986; Imoto *et al.*, 1988; Leonard *et al.*, 1988). As Figures 11 and 12 illustrate, this helix is not straight, but bends near the middle of the bilayer, where it comes closest to the axis of the pore, and tilts radially outwards on either side. While the limited resolution does not allow the true nature of this curvature to be described, it seems to entail quite an abrupt change of angle and hence is referred to below as a kink. α-Helices in a number of enzymes are kinked around amino acid residues contributing to the structure of the active site (Barlow & Thornton, 1988).

The distance of the helix from the centre of the pore at the level of the kink cannot be estimated accurately, since the rod at this point is not distinct. A simple extrapolation would place it about 11 Å away (Fig. 12a), but partial unfolding in this region may allow an even closer approach.

(e) *Tentative alignment of M2 sequence with the map*

Figure 13 shows the amino acid sequence around M2 (*Torpedo* α subunit) and the channel in profile

with the positions of the M2 rods superimposed. An approximate alignment of the sequence with the three-dimensional densities can be made because the lower portions of the M2 helices of all of the subunits have a distinctive pattern of small residues alternating with bulky hydrophobic side-chains; this pattern extends over a distance of two to three turns and should therefore be visible at 9 Å resolution. The small residues involved (Ser, Ala, Thr and Gly) occupy only 40 to 75% of the volume of the neighbouring hydrophobic side-chains. The upper portion in contrast, is composed mainly of hydrophobic side-chains which are evenly distributed around the helix.

As shown in Figure 13b, the small residues line up along one face of the helix (broken line). This face is inclined to the helix axis such that flanking large hydrophobic side-chains (dotted line) pointing towards the pore at the top end will have moved over to the (left) side at the bottom end, where the small residues would now be facing the pore. This changing distribution of mass on the helix surface accounts qualitatively for the slewing to the left of the densities around the pore (Fig. 12b), the changing shape of the rods, and the openness of the pore at the cytoplasmic headgroups (Fig. 12c): features that all lie below the kink (Fig. 11c). On the other hand, the upper portion of M2, containing the even distribution of hydrophobic side-chains, correlates with the region where the rods have an approximately circular cross-section; that is the region above the kink (Fig. 11b). Hence, based on the appearance of the rods, the point at which the sequence changes character (arrow in Fig. 13b) aligns approximately with the kink.

Alternatively, the alignment may be obtained by assuming that the portion of the sequence containing the inclined lines of large and small residues (shaded bar in Fig. 13b) corresponds to the stretch along the rods over which the densities are most strongly slewed (line in Fig. 12b). The kink lies just below the upper end of this stretch (Fig. 12a) and therefore at the level denoted by the arrow in the sequence (Fig. 13b).

Identification of the stretch on M2 corresponding to the bilayer-spanning segment (rectangle in Fig. 13b) follows automatically, because the two phospholipid headgroup regions and the kink are at measurable distances from each other (Fig. 13a).

(f) *Charged amino acids at bilayer surface*

The validity of the above estimate for the location of the bilayer-spanning segment on M2 is reinforced by the observation that it places the charged glutamic acid and lysine residues on either side of the bilayer (Fig. 13b), with no charged groups at levels within the hydrophobic core. The aligned sequences of the other subunits, and also of the subunits of other members of the acetylcholine receptor family, follow the same pattern (Table 4). Such a symmetrical organization of the charged groups might arise because it is energetically favoured during assembly, avoiding their exposure to the hydrophobic fatty acid chains of the lipid. The complete absence of charged groups inside the hydrophobic core of the bilayer is a feature of the structure of the photosynthetic reaction centre (Michel & Deisenhofer, 1987).

The two glutamic acid residues bracketing the bilayer are components of the extracellular and intermediate rings of negative charge, which affect ion flow (Imoto *et al.*, 1988). The third, cytoplasmic ring, which has a weak effect on ion flow, is not bracketing the bilayer according to the alignment, but is in the cytoplasmic part of the structure.

(g) *The gate of the channel*

The density along the axis of the pore is highest near the middle of the bilayer (Fig. 12c), at the level of the kink (Fig. 12a). This site, 50 Å below the putative acetylcholine binding site (Fig. 9), must be where the channel is blocked in this closed conformation of the receptor. In fact, the kinked part of the M2 helix is the only part of the whole molecule sufficiently close to the axis that candidate side-chains could approach the centre of the pore.

The probable side-chains implicated, according to the alignment above, and its proximity to the pore surface (see below), are those of Leu251 on the α subunits (cross in Fig. 13b) and the leucine residues at homologous positions on the other subunits. Nearby serine (or in some cases alanine) residues, which have just over half the volume of a leucine residue, would not account for the density on the axis of the pore. An alignment with the helix shifted up or down by one turn gives a slightly poorer match with the three-dimensional map, and would entail an asymmetric disposition of charged groups on either side of the bilayer.

Figure 14 shows how the gate of the closed channel might be constructed, based on the involvement of the leucine residues. It suggests that the leucine residues project in from the five encircling kinks towards the centre of the pore and associate by side to side interactions of their branched side-chains. A tight hydrophobic ring would thereby be created, making a barrier that the hydrated ions would be unable to cross. A tight ring is consistent with the structural details, since leucine residues project 7 to 8 Å from the axis of a helix (Richmond & Richards, 1978), and must therefore come very close to the centre of the pore.

Side to side association of leucine residues, from pairs of helices pointing in the same direction, occurs in the formation of leucine zippers (O'Shea *et al.*, 1991), and it seems that a similar association could underlie the switch between open and closed states of a channel. In the leucine zipper family of DNA-binding proteins, the stability of the association is usually weak, and is affected by nearby hydrophobic and electrostatic interactions (Alber, 1992). One would expect a similar situation to apply in the case of a channel.

Table 4

Charged amino acids (circled) and conserved leucine (boxed) on M2 in relation to estimated position of bilayer

Torpedo, α (1)	G	(E)	(K)	M	T	L	S	I	S	V	L	[L]	S	L	T	V	F	L	L	V	I	V	(E)	L
Torpedo, β (2)	G	(E)	(K)	M	S	L	S	I	S	A	L	[L]	A	T	V	V	F	L	L	L	L	A	(D)	(K)
Torpedo, γ (3)	G	Q	(K)	C	T	L	S	I	S	V	L	[L]	A	Q	T	I	F	L	F	L	I	A	Q	(K)
Torpedo, δ (2)	G	(E)	(K)	M	S	T	A	I	S	V	L	[L]	A	Q	A	V	F	L	L	L	T	S	Q	(R)
N. AchR, α2 (4)	G	(E)	(K)	I	T	L	C	I	S	V	L	[L]	S	L	T	V	F	L	L	L	I	T	(E)	I
N. AchR, β2 (5)	G	(E)	(K)	M	T	L	C	I	S	V	L	[L]	A	L	T	V	F	L	L	L	I	S	(K)	I
$GABA_A$ R, α1 (6)	P	A	(R)	T	V	F	G	V	T	T	V	[L]	T	M	T	T	L	S	I	S	A	(R)	N	S
$GABA_A$ R, β1 (6)	A	A	(R)	V	A	L	G	I	T	T	V	[L]	T	M	T	T	I	S	T	H	L	(R)	(E)	T
Glycine R, α1 (7)	P	A	(R)	V	G	L	G	I	T	T	V	[L]	T	M	T	T	Q	S	S	G	S	(R)	A	S
Glycine R, β1 (8)	A	A	(R)	V	P	L	G	I	F	S	V	[L]	S	L	A	S	(E)	C	T	T	L	A	A	(E)
5HT3 R (9)	G	(E)	(R)	V	S	F	(K)	I	T	L	L	[L]	G	Y	S	V	F	L	I	V	S	(D)	T	L

bilayer

References: (1) Noda *et al.* (1982); (2) Noda *et al.* (1983*a*); (3) Noda *et al.* (1983*b*); (4) Wada *et al.* (1988); (5) Deneris *et al.* (1988); (6) Scholfield *et al.* (1987); (7) Grenningloh *et al.* (1987); (8) Grenningloh *et al.* (1990); (9) Maricq *et al.* (1991).

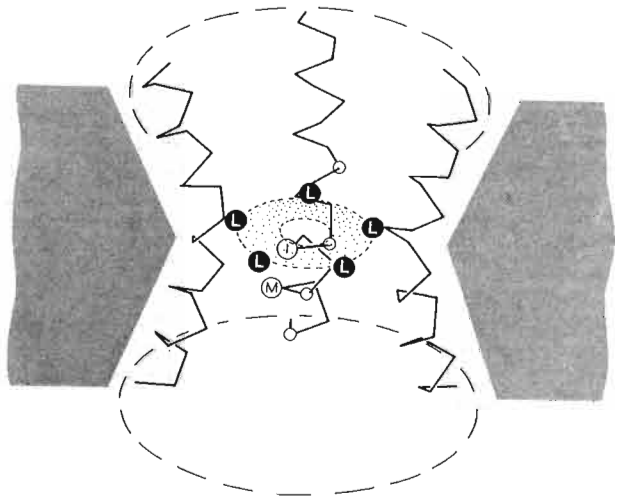

Figure 14. A diagram illustrating how the gate of the closed channel might be constructed. The M2 helix, which is kinked about halfway across the bilayer, allows leucine side-chains (L) to project in close to the centre of the pore. The leucine residues associate by side to side interaction of their branched side-chains, forming a tight hydrophobic ring. The ring makes a barrier that hydrated ions are unable to cross. Adjacent to, and below, the leucine residues is a sloping line of small residues (small circles), flanked by large hydrophobic side-chains, some of which are indicated (large circles). See also Fig. 13b.

(h) *Importance of Leu251*

Several other arguments can be made that this leucine residue at least occupies a critical position in relation to the pore. First, it is the most conserved residue in the M2 sequence, being present at the same position on almost all subunits of all members of the acetylcholine receptor family (Unwin, 1989; Table 4). Second, it is located on the helix (Fig. 14) beside a line of small polar residues (dots in Fig. 13b), which when mutated affect binding of the open channel blocker, QX-222 (Leonard *et al.*, 1988; Charnet *et al.*, 1990) and ion flow through the pore (Villarroel *et al.*, 1991; Villarroel & Sakmann, 1992). Third, its close proximity to the pore-lining surface is implied by the accessibility of the β and γ subunit leucine residues to the photoactivable reagent chlorpromazine when reacted with the receptor and agonist under equilibium conditions (Giraudat *et al.*, 1987; Revah *et al.*, 1990). Fourth, mutation of this leucine residue to residues of different size and polarity in homomeric neuronal α-7 acetylcholine receptors affects profoundly their pharmacological properties (Revah *et al.*, 1991; Bertrand *et al.*, 1992), suggesting that the leucine residue may play an important functional role as well as influencing ion transport through the pore.

(i) *Relation to open state*

The small residues important for binding QX-222 (upper 2 dots in Fig. 13b), when mutated, do not much affect ion flow through the pore, whereas the remaining residue (Thr244 on the *Torpedo* α subunit; bottom dot in Fig. 13b) either restricts or enhances ion flow, depending on the volume of the substituted residue (Villarroel *et al.*, 1991; Villarroel & Sakmann, 1992). Therefore, the point of maximum constriction in the open channel appears to be closer to Thr244 than to Leu251. This suggests that some flexure of M2 could be involved in the transition between the two states. In any event, it appears that the open pore would have a fairly short constriction zone (Dani, 1989), which may be similar in extent to that found in porin (~9 Å; Cowan *et al.*, 1992).

(j) *Prospects for future work*

While the methods used in the present study have led to a significant improvement in resolution over that in the earlier work, the images are still poor compared to what is theoretically attainable. The ctf modulations at the limits of the Fourier transforms ($1/8{\cdot}7$ Å^{-1}) are typically about one-fifth of their strength at low resolution whereas, according to the fall-off with angle of the atomic scattering amplitudes, the attenuation should be negligible. Several factors may have contributed to the loss in contrast at the finer spacings. First, there is localized motion of the ice-embedded material, resulting from inelastic collisions by the incident electrons. Second, it can be shown that the curvature of the Ewald sphere leads to significant weakening of the highest resolution Fourier terms from specimens as thick as the tubes. Third, there is loss of contrast, due to partial coherence, in images that were strongly defocussed. Fourth, there is a variable degradation associated with the limited stability of the cold stage.

The best image overall was that recorded at 200 kV, with a high coherence, field emission source. The layer-lines from this image had smaller departures from centrosymmetric phases, especially at higher resolution, than did the layer-lines from the other (120 kV) images. Such an improvement may have been aided by the greater coherence of the electron source. But the higher accelerating voltage is an important factor, since it reduces the total amount of inelastic scattering by lowering the probability of electrons that have been elastically scattered undergoing subsequent inelastic events. Also, at 200 kV, the effect of curvature of the Ewald sphere is less.

As yet then, the resolution is limited by technical factors rather than by some inherent property of the specimen. The use of higher voltage field emission microscopes and more stable cold stages should bring about major improvements in the quality of the images. So it ought to be possible in the near future to derive from the tubes a more precise picture of the putative acetylcholine binding pocket, the gate and the structure surrounding these basic functional domains.

5. Conclusions

The structure of the acetylcholine receptor, in the closed conformation, has been determined to a resolution of 9 Å by averaging data from images of tubes in ice, using helical diffraction methods of analysis. The helical symmetry of the specimen has enabled approximately equal resolution to be attained in all directions.

Rods have been resolved in equivalent 5-fold positions that probably correspond to α-helices. In the synaptic part of each subunit, about 30 Å above the bilayer surface, there is a group of three rods oriented predominantly perpendicular to the plane of the bilayer, which twist around each other as in a left-handed coil. The distinctive appearance of the α subunits in this region suggests that the rods may be involved in forming the binding pocket for acetylcholine. In the bilayer-spanning part there is only one rod clearly visible, which forms the wall lining the pore. It is rimmed on its lipid-facing sides by a continuous density, which may be β-sheet.

The rod lining the pore bends, or kinks, near its mid-point, constricting the channel near the middle of the bilayer. A tentative alignment of three-dimensional features of the rod with the sequence of the pore-lining segment, M2, suggests that the side-chains of a highly conserved leucine residue may project into the pore from the five encircling kinks to create the barrier that ions cannot cross.

I am grateful to many colleagues at the MRC Laboratory and at the Scripps Research Institute, La Jolla, for their help, encouragement, and support. Philips Electron Optics generously allowed me to use their 200 kV field emission microscope at the factory, in Eindhoven. The research was supported, in part, by a grant (GM44149) from the National Institutes of Health.

References

Akabas, M. H., Stauffer, D. A., Xu, M. & Karlin, A. (1992). Acetylcholine receptor channel structure probed in cysteine-substitution mutants. *Science*, **258**, 307–310.

Alber, T. (1992). Structure of the leucine zipper. *Curr. Op. Gen. Develop.* **2**, 205–210.

Amos, L. A. & Klug, A. (1975). Three-dimensional image reconstructions of the contractile tail of T4 bacteriophage. *J. Mol. Biol.* **99**, 51–73.

Barlow, D. J. & Thornton, J. M. (1988). Helix geometry in proteins. *J. Mol. Biol.* **201**, 601–619.

Bertrand, D., Devillers-Thiery, A., Revah, F., Galzi, J.-L., Hussy, N., Mulle, C., Bertrand, S., Ballivet, M. & Changeux, J. P. (1992). Unconventional pharmacology of a neuronal nicotinic receptor mutated in the channel domain. *Proc. Nat. Acad. Sci., U.S.A.* **89**, 1261–1265.

Bon, F., Lebrun, E., Gomel, J., Van Rappenbusch, R., Cartaud, J., Popot, J.-L. & Changeux, J.-P. (1984). Image analysis of the heavy form of the acetylcholine

receptor from *Torpedo marmorata*. *J. Mol. Biol.* **176**, 205–237.

Brisson, A. & Unwin, P. N. T. (1984). Tubular crystals of acetylcholine receptor. *J. Cell Biol.* **99**, 1202–1211.

Brisson, A. & Unwin, P. N. T. (1985). Quaternary structure of the acetylcholine receptor. *Nature (London)*, **315**, 474–477.

Charnet, P., Labarca, C., Leonard, R. J., Vogelaar, N. J., Czyzyk, Gowin, A., Davidson, N. & Lester, H. A. (1990). An open channel blocker interacts with adjacent turns of α-helices in the nicotinic acetylcholine receptor. *Neuron*, **2**, 87–95.

Chothia, C. (1984). Principals that determine the structure of proteins. *Annu. Rev. Biochem.* **53**, 537–572.

Claudio, T. (1989). Molecular genetics of acetylcholine receptor channels. In *Frontiers in Molecular Biology: Molecular Neurobiology* (Glover, D. M. & Hames, B. D., eds), pp. 63–142, IRL Press, Oxford.

Cowan, S. W., Schirmer, T., Rummel, G., Steiert, M., Ghosh, R., Pauptit, R. A., Jansonius, J. N. & Rosenbusch, J. P. (1992). Crystal structures explain functional properties of two *E. coli* porins. *Nature (London)*, **358**, 727–733.

Dani, J. A. (1989). Open channel structure and ion binding site of the nicotinic acetylcholine receptor channel. *J. Neurosci.* **9**, 884–892.

Deneris, E. S., Connolly, J., Boulter, J., Wada, E., Wada, K., Swanson, A. W., Patrick, J. & Heinemann, S. (1988). Primary structure of β-2: a novel subunit of neuronal nicotinic acetylcholine receptors. *Neuron*, **1**, 45–54.

Dennis, M., Giraudat, J., Kotzbya-Hibert, F., Goeldner, M., Hirth, C., Chang, J.-Y. & Changeux, J.-P. (1986). A photoaffinity ligand of the acetylcholine-binding site predominantly labels the region 179–207 of the α-subunit on native acetylcholine receptor from *Torpedo marmorata*. *FEBS Letters*, **207**, 243–249.

Dennis, M., Giraudat, J., Kotzbya-Hibert, F., Goeldner, M., Hirth, C., Chang, J.-Y., Lazure, C., Chrétien, M. & Changeux, J.-P. (1988). Amino acids of the *Torpedo marmorata* acetylcholine receptor α subunit labelled by a photoaffinity ligand for the acetylcholine binding site. *Biochemistry*, **27**, 2346–2357.

DeRosier, D. J. & Klug, A. (1968). Reconstruction of three-dimensional structures from electron micrographs. *Nature (London)*, **217**, 130–134.

DeRosier, D. J. & Moore, P. B. (1970). Reconstruction of three-dimensional images from electron micrographs of structures with helical symmetry. *J. Mol. Biol.* **52**, 355–369.

DiPaola, M., Kao, P. N. & Karlin, A. (1990). Mapping the α-subunit site photolabelled by the non competitive inhibitor quinacrine azide in the active state of the nicotinic acetylcholine receptor. *J. Biol. Chem.* **265**, 11017–11029.

Frank, J. (1973). The envelope of the electron microscopic transfer function for partially coherent illumination. *Optik*, **38**, 519–536.

Galzi, J.-L., Revah, F., Black, D., Goeldner, M., Hirth, C. & Changeux, J.-P. (1990). Identification of a novel amino acid α-tyrosine 93 within the cholinergic ligands-binding sites of the acetylcholine receptor by photoaffinity labelling. *J. Biol. Chem.* **265**, 10430–10437.

Galzi, J.-L., Revah, F., Bessis, A. & Changeux, J.-P. (1991). Functional architecture of the nicotinic acetylcholine receptor: from electric organ to brain. *Annu. Rev. Pharmacol.* **31**, 37–72.

Giraudat, J., Dennis, M., Heidmann, T., Chang, J.-Y. & Changeux, J.-P. (1986). Structure of the high-affinity binding site for noncompetitive blockers of the acetylcholine receptor: serine-262 of the δ subunit is labeled by [^{3}H]chlorpromazine. *Proc. Nat. Acad. Sci., U.S.A.* **83**, 2719–2723.

Giraudat, J., Dennis, M., Heidmann, T., Haumont, P.-Y., Lederer, F. & Changeux, J.-P. (1987). Structure of the high affinity binding site for noncompetitive blockers of the acetylcholine receptor: [^{3}H]chlorpromazine labels homologous residues in the β and δ-chains. *Biochemistry*, **26**, 2410–2418.

Grenningloh, G., Rienitz, A., Schmitt, B., Methfessel, C., Zensen, M., Beyreuther, K., Gundelfinger, E. D. & Betz, H. (1987). The strychnine-binding subunit of the glycine receptor shows homology with the nicotinic acetylcholine receptor. *Nature (London)*, **328**, 215–220.

Grenningloh, G., Pribilla, I., Prior, P., Multhaup, G., Beyreuther, K., Taleb, O. & Betz, H. (1990). Cloning and expression of the 58kd β subunit of the inhibitory glycine receptor. *Neuron*, **4**, 963–970.

Henderson, R. & Unwin, P. N. T. (1975). Three-dimensional model of purple membrane obtained by electron microscopy. *Nature (London)*, **257**, 28–32.

Henderson, R., Baldwin, J. M., Ceska, T. A., Zemlin, F., Beckmann, E. & Downing, K. (1990). A model for the structure of bacteriorhodopsin based on high resolution electron cryo-microscopy. *J. Mol. Biol.* **213**, 899–929.

Herz, J. M., Johnson, D. A. & Taylor, P. (1989). Distance between the agonist and noncompetitive inhibitor sites on the nicotinic acetylcholine receptor. *J. Biol. Chem.* **264**, 12439–12448.

Hessler, D., Young, S. J., Carragher, B. O., Martone, M., Hinshaw, J. E., Milligan, R. A., Masliah, E., Whittaker, M., Lamont, S. & Ellisman, M. H. (1992). SYNU: software for visualization of 3-dimensional biological structures. In *Microscopy: The Key Research Tool* (Lymm, C. E., Peachey, L. D. & Fisher, R. M., eds), pp. 72–82, EMSA Milwaukee.

Hucho, F., Oberthur, W. & Lottspeich, F. (1986). The ion channel of the nicotinic acetylcholine receptor is formed by the homologous helices MII of the receptor subunits. *FEBS Letters*, **205**, 137–142.

Imoto, K., Busch, C., Sakmann, B., Mishina, M., Konno, T., Nakai, J., Bujo, H., Mori, Y., Fukuda, K. & Numa, S. (1988). Rings of negatively charged amino acids determine the acetylcholine receptor channel conductance. *Nature (London)*, **335**, 645–648.

Jeng, T.-W., Crowther, R. A., Stubbs, G. & Chiu, W. (1989). Visualization of α helices in TMV by cryo-electron microscopy. *J. Mol. Biol.* **205**, 251–257.

Karlin, A. (1991). Explorations of the nicotinic acetylcholine receptor. *The Harvey Lectures, Series*, **85**, 71–107.

Kistler, J. & Stroud, R. M. (1981). Crystalline arrays of membrane-bound acetylcholine receptor. *Proc. Nat. Acad. Sci., U.S.A.* **78**, 3678–3682.

Kistler, J., Stroud, R. M., Klymkowsky, M. W., Lalancette, R. A. & Fairclough, R. H. (1982). Structure and function of an acetylcholine receptor. *Biophys. J.* **37**, 371–383.

Klug, A., Crick, F. H. C., & Wykoff, H. W. (1958). Diffraction by helical structures. *Acta Crystallogr.* **11**, 199–213.

Kubalek, E., Ralston, S., Lindstrom, J. & Unwin, N. (1987). Location of subunits within the acetylcholine

receptor by electron image analysis of tubular crystals from *Torpedo marmorata*. *J. Cell Biol.* **105**, 9–18.

LaRochelle, W. J. & Froehner, S. C. (1986). Determination of the tissue distributions and relative concentrations of the post-synaptic 43-kDa protein and the acetylcholine receptor in *Torpedo*. *J. Biol. Chem.* **261**, 5270–5274.

Leonard, R. J., Labarca, C. G., Charnet, P., Davidson, N. & Lester, H. A. (1988). Evidence that the M2 membrane-spanning region lines the ion channel pore of the nicotinic receptor. *Science*, **242**, 1578–1581.

Maricq, A. V., Peterson, A. S., Brake, A. J., Myers, R. M. & Julius, D. (1991). Primary structure and functional expression of the 5HT3 receptor, a serotonin-gated ion channel. *Science*, **254**, 432–437.

Michel, H. & Deisenhofer, J. (1987). The photosynthetic reaction centre from the purple bacterium *Rhodopseudomonas viridis*. *Chem. Scripta*, **27B**, 173–180.

Mielke, D. L. & Wallace, B. A. (1988). Secondary structural analyses of the nicotinic acetylcholine receptor as a test of molecular models. *J. Biol. Chem.* **263**, 3177–3182.

Mitra, A. K., McCarthy, M. P. & Stroud, R. M. (1989). Three-dimensional structure of the nicotinic acetylcholine receptor and location of the major associated 43-kD cytoskeletal protein, determined at 22 Å by low dose electron microscopy and X-ray diffraction to 12·5 Å. *J. Cell Biol.* **109**, 755–774.

Moody, M. F. (1990). Image analysis of electron micrographs. In *Biophysical Electron Microscopy*, pp. 145–287, Academic Press Ltd, London.

Neubig, R. R. & Cohen, J. B. (1979). Equilibrium binding of [^{3}H]tubocurarine and [^{3}H]acetylcholine by *Torpedo* postsynaptic membranes: stoichiometry and ligand interactions. *Biochemistry*, **18**, 5464–5475.

Noda, M., Takahashi, H., Tanabe, T., Toyosato, M., Furutani, Y., Hirose, T., Asai, M., Inayama, S., Miyata, T. & Numa, S. (1982). Primary structure of the α subunit precursor of *Torpedo californica* acetylcholine receptor deduced from cDNA sequence. *Nature (London)*, **299**, 793–797.

Noda, M., Takahashi, H., Tanabe, T., Toyosato, M., Kikyotani, S., Hirose, T., Asai, M., Takashima, H., Inayama, S., Miyata, T. & Numa, S. (1983*a*). Primary structures of β- and δ-subunit precursors of *Torpedo californica* acetylcholine receptor deduced from cDNA sequences. *Nature (London)*, **301**, 251–255.

Noda, M., Takahashi, H., Tanabe, T., Toyosato, M., Kikyotani, S., Furutani, Y., Hirose, T., Takashima, H., Inayama, S., Miyata, T. & Numa, S. (1983*b*). Structural homology of *Torpedo californica* acetylcholine receptor subunits. *Nature (London)*, **302**, 528–532.

O'Shea, E. K., Klemm, J. D., Kim, P. S. & Alber, T. (1991). X-ray structure of the GCN4 leucine zipper, a two-stranded, parallel coiled coil. *Science*, **254**, 539–544.

Pedersen, S. E. & Cohen, J. B. (1990). d-Tubocurarine binding sites are located at α-γ and α-δ subunit interfaces of the nicotinic acetylcholine receptor. *Proc. Nat. Acad. Sci., U.S.A.* **87**, 2785–2789.

Pedersen, S. E., Sharp, S. D., Liu, W.-S. & Cohen, J. B. (1992). Structure of the non-competitive antagonist-binding site of the *Torpedo* nicotinic acetylcholine receptor. [^{3}H]Meproadifen mustard reacts selectively with α-subunit Glu-262. *J. Biol. Chem.* **267**, 10489–10499.

Revah, F., Galzi, J. L., Giraudat, J., Haumant, P. Y., Lederer, F. & Changeux, J.-P. (1990). The non-competitive blocker [^{3}H]chlorpromazine labels three amino acids of the acetylcholine receptor γ subunit: implications for the α-helical organization of regions MII and for the structure of the ion channel. *Proc. Nat. Acad. Sci., U.S.A.* **87**, 4675–4679.

Revah, F., Bertrand, D., Galzi, J.-L., Devillers-Thiery, A., Mulle, C., Hussy, N., Bertrand, S., Ballivet, M. & Changeux, J.-P. (1991). Mutations in the channel domain alter desensitization of a neuronal acetylcholine receptor. *Nature (London)*, **353**, 846–849.

Richmond, T. J. & Richards, F. M. (1978). Packing of α-helices: geometrical constraints and contact areas. *J. Mol. Biol.* **119**, 537–555.

Ross, M. J., Klymkowski, M. W., Agard, D. A. & Stroud, R. M. (1977). Structural studies of a membrane-bound acetylcholine receptor from *Torpedo californica*. *J. Mol. Biol.* **116**, 635–659.

Saxton, W. O. (1978). *Computer Techniques for Image Processing in Electron Microscopy*. Academic Press, New York.

Schofield, P. R., Darlison, M. G., Fujita, N., Burt, D. R., Stephenson, F. A., Rodriguez, H., Rhee, L. M., Ramachandran, J., Reale, V., Glencorse, T. A., Seeburg, P. H. & Barnard, E. A. (1987). Sequence and functional expression of the $GABA_A$ receptor shows a ligand-gated receptor super-family. *Nature (London)*, **328**, 221–227.

Sixma, T. K., Pronk, S. E., Kalk, K. H., Wartna, E. S., van Zanten, B. A. M., Witholt, B. & Hol, W. G. J. (1991). Crystal structure of a cholera toxin-related heat-labile enterotoxin from *E. coli*. *Nature (London)*, **351**, 371–377.

Stein, P. E., Boodhoo, A., Tyrrell, G. J., Brunton, J. L. & Read, R. J. (1992). Crystal structure of the cell-binding B oligomer of verotoxin-1 from *E. coli*. *Nature (London)*, **355**, 748–750.

Sussmann, J. L., Harel, M., Frolow, F., Oefner, C., Goldman, A., Toker, L. & Silman, I. (1991). Atomic structure of acetylcholinesterase from *Torpedo marmorata*: a prototypic acetylcholine-binding protein. *Science*, **253**, 872–878.

Thon, F. (1966). Zur Defokussierungsabhängigkeit des Phasen-kontrastes bei der elektronenmikroskopischen Abbildung. *Z. Naturforsch.* **219**, 476–478.

Toyoshima, C. (1989). On the use of holey grids in electron crystallography. *Ultramicroscopy*, **30**, 439–444.

Toyoshima, C. & Unwin, N. (1988*a*). Ion channel of acetylcholine receptor reconstructed from images of postsynaptic membranes. *Nature (London)*, **336**, 247–250.

Toyoshima, C. & Unwin, N. (1988*b*). Contrast transfer for frozen-hydrated specimens: determination from pairs of defocused images. *Ultramicroscopy*, **25**, 279–292.

Toyoshima, C. & Unwin, P. N. T. (1990). Three-dimensional structure of the acetylcholine receptor by cryoelectron microscopy and helical image reconstruction. *J. Cell Biol.* **111**, 2623–2635.

Unwin, N. (1989). The structure of ion channels in membranes of excitable cells. *Neuron*, **3**, 665–676.

Unwin, P. N. T. & Henderson, R. (1975). Molecular structure determination by electron microscopy of unstained crystalline specimens. *J. Mol. Biol.* **94**, 425–440.

Unwin, N., Toyoshima, C. & Kubalek, E. (1988).

Arrangements of the acetylcholine receptor subunits in the resting and desensitized states, determined by cryoelectron microscopy of crystallized *Torpedo* postsynaptic membranes. *J. Cell Biol.* **107**, 1123–1138.

Villarroel, A. & Sakmann, B. (1992). Threonine in the selectivity filter of the acetylcholine receptor channel. *Biophys. J.* **62**, 196–205.

Villarroel, A., Herlitze, S., Koenen, M. & Sakmann, B. (1991). Location of a threonine residue in the α subunit M2 transmembrane segment that determines the ion flow through the acetylcholine receptor channel. *Proc. Roy. Soc. ser. B,* **243**, 69–74.

Wada, K., Ballivet, M., Boulter, J., Connolly, J., Wada, E., Deneris, E. S., Swanson, L. W., Heinemann, S. & Patrick, J. (1988). Functional expression of a new pharmacological subtype of brain nicotinic acetylcholine receptor. *Science*, **240**, 330–334.

Weiss, M. S., Abele, U., Weckesser, J., Welte, W., Schiltz, E. & Schultz, G. E. (1991). Molecular architecture and electrostatic properties of a bacterial porin. *Science*, **254**, 1627–1630.

Zingsheim, H. P., Neugebauer, D.-C. & Barrantes, F. J. (1980). Structural details of membrane-bound acetylcholine receptor from *Torpedo marmorata*. *Proc. Nat. Acad. Sci., U.S.A.* **73**, 952–956.

Edited by D. DeRosier